KERNFORSCHUNGSANLAGE JÜLICH GmbH

Institut für Reaktorentwicklung

An Investigation of Fission Models for High-Energy Radiation Transport Calculations

by

T. W. Armstrong, P. Cloth, D. Filges, R. D. Neef

Jül - 1859
July 1983
ISSN 0366-0885

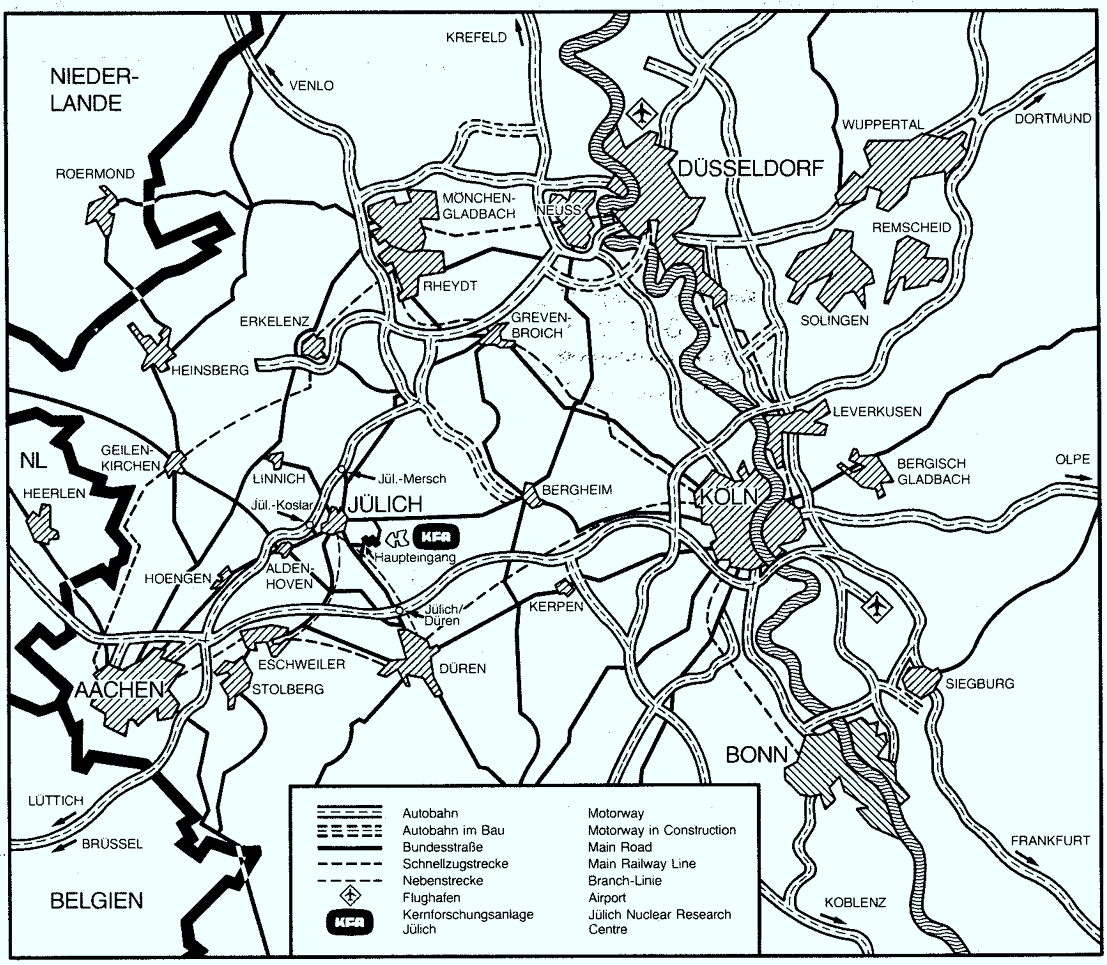

Als Manuskript gedruckt

Berichte der Kernforschungsanlage Jülich – Nr. 1859

Institut für Reaktorentwicklung Jül - 1859

Zu beziehen durch: ZENTRALBIBLIOTHEK der Kernforschungsanlage Jülich GmbH

Postfach 1913 · D-5170 Jülich (Bundesrepublik Deutschland)

Telefon: 02461/610 · Telex: 833556-0 kf d

An Investigation of Fission Models for High-Energy Radiation Transport Calculations

by

T. W. Armstrong*, P. Cloth, D. Filges, R. D. Neef

Institut für Reaktorentwicklung
Kernforschungsanlage Jülich GmbH, Germany

*KFA Consultant, P.O. Box 2807
La Jolla, California 92938, USA

ABSTRACT

An investigation of high-energy fission models for use in the HETC code has been made. The validation work has been directed checking the accuracy of the high-energy radiation transport computer code HETC to investigate the appropriate model for routine calculations, particularly for spallation neutron source applications.

Model calculations are given in terms of neutron production, fission fragment energy release, and residual nuclei production for high-energy protons incident on thin uranium targets. The effect of the fission models on neutron production from thick uranium targets is also shown.

CONTENTS

1 INTRODUCTION

As part of a German study (designated SNQ, for "Spallations Neutronen Quelle") to examine concepts for using high-energy proton beams to produce intense thermal neutron beams for solid state physics research, several investigations (e.g., /1/) have been made to evaluate the accuracy of present theoretical methods and physics models available for various predictions related to target station design. In particular, most of this validation work has been directed toward checking the accuracy of the high-energy radiation transport computer code HETC /2/, which is being used for various estimates (neutron output, heating, induced radioactivity, etc.) related to assessing alternative design options for the SNQ target. As part of this validation work, an investigation of high-energy fission models for use in the HETC code has been made, and this is the subject of the present report. Some of the results presented here have been given previously at meetings of the ICANS (International Collaboration on Advanced Neutron Sources) group.

High-energy fission becomes an important nuclear interaction mechanism for nucleon collisions $\gtrsim$ 100 MeV with high-mass target nuclei, in which case there is competition between fission and evaporation at each step of the nuclear de-excitation process. For example, for high-energy proton collisions with uranium, fission occurs about 80 % of the time at some stage in the de-excitation chain. Statistical models can be applied to determine the parameters for the fission fragments immediately after fission, and the usual evaporation model applied to determine post-fission particle emission from each fragment. In recent years, several high-energy fission models /3-6/ have been developed for the HETC code, and the overall objective here is to investigate the appropriate model for routine HETC calculations, particularly for spallation neutron source applications.

If fission occurs, the following quantities for the outcome of the collision are expected to be different compared to spallation without fission: (a) energy deposition, (b) mass and charge distributions for the residual nuclei, (c) neutron multiplicity, and (d) neutron spectrum. There are clearly large differences in these first two items if fission takes place. The magnitude and spectral difference in neutron production, and the resulting influence on the thick-target thermal neutron flux of interest for spallation neutron sources, is not well-determined. Thus, the effects of high-energy fission on neutron production, and the thermal neutron flux generated, is the main emphasis of the calculations and model comparisons made here.

The basic features of the fission models that have been developed for HETC are summarized in Section 2. For most of the calculations made in this study, a fission model developed at the Rutherford Appleton Laboratory has been used, and a detailed discussion of this model is given in Section 2.

In Section 3, model comparisons of neutron production and residual mass distributions are given for protons incident on thin uranium targets. By "thin targets" we mean target thicknesses sufficiently small that the secondary particles created escape from the target without undergoing further collisions, so the results are for a single proton collision. Thus, such thin target comparisons are appropriate for identifying basic differences in nuclear collision model predictions.

To assess the practical importance of nuclear model differences for spallation source applications, thick targets must be considered. The results from thick target irradiation, such as the neutron flux, represent the cummulative effect of collisions initiated by primary beam particles and secondary particles (neutrons, protons, and pions) over a wide range of energies. Therefore, we have also made thick target calculations to compare the neutron production and thermal neutron flux spatial distribution for various fission model parameter assumptions, and these results are given in Section 4.

In Section 5 a summary of the study conclusions is given.

2 HIGH-ENERGY FISSION PROCESS AND MODELS

Without fission, spallation collisions can be treated as a two-step process: (a) an intranuclear cascade, described by a series of independent particle-particle collisions inside the nucleus, and (b) subsequent de-excitation by a series of particle emissions, which can be described by an evaporation model. For very heavy nuclei, there is competition between evaporation and fission at each step of the de-excitation sequence. The probability of fission at some step during de-excitation in high-energy ($\gtrsim$ 100 MeV) collisions is proportional to Z^2/A of the target nucleus. For example, $\sigma_f/\sigma_t \sim 0.05$ for lead and $\sigma_f/\sigma_t \sim 0.8$ for uranium.

As illustrated in Fig. 1, the information which must be determined by the fission model is the probability of fission at each step and the parameters of the fission fragments immediately after fission, which are then used as input for a post-fission evaporation calculation for each fragment.

In this section we give an overview of several fission models which have been developed for thick target radiation transport applications (Section 2.1), and a summary of some previous validation studies which have been made using these models (Section 2.2). Almost all of the results given later in Sections 3 and 4 for calculations made at KFA were obtained using the Rutherford Appleton Laboratory model, so some details of this model are given in Section 2.3.

2.1 Basic Features of Fission Models

Recently, there have been two high-energy fission models developed for use in the thick-target nucleon-meson transport code HETC: one by Atchison at the Rutherford Appleton Laboratory (RAL) /3/, and one by Alsmiller, et.al., at the Oak Ridge National Laboratory (ORNL) /4/. Also, Takahashi at Brookhaven National Laboratory (BNL) /5/ and Nakahara at the Japan Atomic Energy Research Institute (JAERI) /6/ have developed high-energy fission models for the NMTC transport code /7/, which is an earlier version of HETC. (Barashenkov, et.al. have also developed a high-energy fission model for use in the Dubna transport code /8/.)

The fundamental basis of all of these models is the statistical model of fission developed by Fong /9/. Basically, the assumption is that the fission process is "slow" (i.e., the nucleus exists in an equilibrium state at any time), so the probability of a particular fission mode (state of the fission fragments) is proportional to the density of quantum states at the time of splitting. From the Fong theory, the fission mode probability is expressed as a function of eleven variables: $N(A_1, A_2, Z_1, Z_2, C, D, K, E, E_1, j_1, j_2)$, where the subscripts denote the fission fragments; A, Z, and j denote mass number, charge number and angular momentum, and the remaining are energy variables (C, Coulomb; D, deformation; K, translational; E, total; and E_1, excitation).

The high-energy fission models developed differ in the approximations made in arriving at a practical implementation of the above general expression and in the physical data used. It is not the purpose here to evaluate these various approximations. Indeed, many of the approximations are interdependent, making judgement of the practical importance of particular assumptions difficult. Therefore, the model comparisons here are in terms of "output" rather than assessment of the intermediate physics. Simple characterizations of the different models are given in Fig. 2.

Also given in Fig. 2 are the values for the parameter B_0 assumed for the different models, which, as shown later, has an important influence on neutron production. This parameter is involved in the evaporation calculation in the following way. From evaporation theory (e.g., /10/), the probability of particle emission of type i with kinetic energy E is expressed as

$$P_i(E) \propto (2S_i+1)\ m_i E \sigma_{ci}(E)\ \omega\ (E^*),$$

with S_i= spin, m_i= mass, and σ_{ci}= cross section for compound nucleus formation in the inverse reaction. The level density for excitation energy E^* is given by

$$\omega\ (E^*) = \omega_0 \exp(2(aE^*-\delta)^{1/2}),$$

where ω_0 and a are constants for a given nucleus and δ is the pairing energy. The level density parameter, a, is given by

$$a = A/B_0(1+Y(A-2Z)^2/A^2),$$

and $Y \sim 1.5$. From various analyses, B_0 is in the range from about 8 to 20 MeV (e.g., /10/).

2.2 Previous Validations

Several thick-target calculations, with and without high-energy fission taken into account, have been made for neutron production and compared with experimental data. Table 1 compares the calculated results of Alsmiller, et al. /11/ using the ORNL fission model and the HETC transport code with data obtained under the FERFICON (Fertile-to-Fission Conversion) measurement program, a collaborative experimental effort between TRIUMF in Canada and LANL in the U.S. These measurements were made for individual depleted uranium rods, having the dimensions indicated in Table 1, as well as for array arrangements containing 37 individual rods. Table 2 summarizes calculated results which have been obtained using the JAERI and BNL fission models with the measurements of Vassil'Kov for a very large natural uranium target.

We conclude from these, and other (e.g., /11,15/), comparisons that the theoretical predictions and measurements that have been made to date agree to within roughly 20 to 30 %, and this general magnitude of agreement for neutron production can be obtained by neglecting high-energy fission. It is difficult to isolate the influence of the high-energy fission models in these thick target comparisons where low-energy fission also contributes to the neutron production.

2.3 RAL Fission Model

The Rutherford Appleton Laboratory fission model written by Atchison is based on several general assumptions:

a. Fission competes at all stages of nuclear de-excitation, with fission probabilities that vary with the nuclear state.

b. Post-fission parameters depend only on the state of the nucleus at the time of fission and not on the previous sequence of events leading to the state of the nucleus at the time of fission.

c. Only binary fission occurs. While ternary and high-order fission have been observed (e.g., /16/), they occur with probabilities which are insignificant for the practical applications of interest here.

d. Nucleons and charge are conserved between the fissioning nucleus and the two fission fragments. Thus, low-energy neutrons are not emitted at the time of fission, but arise either from the de-excitation of the nucleus before fission following the intranuclear cascade, or from the de-excitation of the fission fragments.

Specific assumptions used in the RAL model to determine the fission probability and post-fission parameters are given below.

Fission Probability

The decision as to whether fission occurs during de-excitation is determined by randomly selecting fission with probability $P_f=(1+\Gamma_n/\Gamma_f)^{-1}$, where Γ_n and Γ_f are the neutron and fission widths, respectively.

For high-Z nuclei in the actinide region, the fission barrier is relatively constant at about 6 MeV, and P_f is not strongly dependent on excitation energy E^* (e.g., Gavron, et.al. /17/). Therefore, the model assumes $P_f=0$ for $E^* \leq 6$ MeV and P_f independent of E^* above 6 MeV, with values determined from the expression of Vandenbosch and Huizenga /18/:

$$\log (\Gamma_n/\Gamma_f) = \Phi(\hat{Z})\ \hat{A} + \psi(\hat{Z})$$

Here $\hat{Z}$ and $\hat{A}$ are the charge and mass numbers of the fissioning nucleus, and Φ and ψ are tabulated functions which depend only on Z. In the code, the above expression is used for $89 \leq \hat{Z} \leq 99$, with fission not considered for higher $\hat{Z}$.

In the sub-actinide region, the results of experiments show that P_f is strongly dependent on E* (e.g., Barashenkov, et.al. /19/), and for the RAL model Atchison has made fits to experimental data using statistical model expressions to determine P_f. Separate fits are made for neutron emission and fission to allow separate level density parameters. The expressions for neutron emission are:

$$\Gamma_n = C_1\ (C_2 I_0 + C_3 A^{1/3} I_1 + A^{2/3}(C_4 I_1 + C_5 I_0))$$

$C_1=0.352 \qquad C_2=1.68 \qquad C_3=1.93$

$C_4=0.76 \qquad C_5=-0.05$

$$I_0=(2a_n)^{-1}\ ((S_n-1.0)\exp(S_n)+1.0)$$

$$I_1=(8a_n^2)^{-1}\ ((2S_n^2-6S_n+6)\exp(S_n)+S_n^2-6)$$

$$a_n=(A-1)/8$$

$$S_n=2(a_n(E^*-B'))^{1/2}$$

B'= separation energy - pairing energy

The expressions used for fission are:

$$\Gamma_f=\ ((S_f-1)\exp(S_f)+1)/a_f$$

$$S_f=2\ (a_f(E^*-E_f))^{1/2}$$

$$E_f=C_6-C_7(Z^2/A)+C_8(Z^2/A)^2$$

$C_6=B'+321.2$ $\quad C_7=16.7$ $\quad C_8=0.218$

$$a_f/a_n=C_9+C_{10}\ ((Z^2/A)-C_{11})^2$$

$C_9=1.09$ $\quad C_{10}=0.011$ $\quad C_{11}=31.09$

The above expressions are used for $Z\leq 88$. The fit parameters for the fission barrier E_f and the level density ratio, a_f/a_n, are based on data for Z<85, so the model fits are used for extrapolation to obtain the fission probability in the Z=85 to 88 region.

Post-Fission Parameters

At this point, fission has occurred for a nucleus having charge $\hat{Z}$, mass $\hat{A}$, excitation energy $\hat{E}^*$, and recoil energy $\hat{E}_r$, and we desire to determine the corresponding parameters for each of the fission fragments.

The selection of the masses for the fission fragments depends on whether the fission is symmetric (a wide, single peak for the fragment mass distribution) or asymmetric (two peaks). For $\hat{Z}^2/\hat{A}\ \leq 35$, only symmetric fission is allowed, and the mass A_1 is selected from a Gaussian distribution of mean $A=\hat{A}/2$ and width $\sigma_A=C_{12}+C_{13}\hat{U}+C_{14}\hat{U}^2$, where $C_{12}=3.97$, $C_{13}=0.425$, $C_{14}=-2.12\times 10^{-3}$, and $\hat{U}$ is the excitation above the fission barrier: $\hat{U}=\hat{E}^*-E_f$. This symmetric fission mass distribution is based on the systematics given by Neuzil and Fairhall /20/. If Z>88, the fission energy barrier is determined in the following way, based on the work of Seaborg and Vandenbosch /21/: $E_f=C_{15}+C_{16}\ \hat{Z}^2/\hat{A}$, where $C_{16}=-0.36$ and C_{15} has the values 18.8, 18.1, 18.1, and 18.5 for odd-odd, even-odd, odd-even, and even-even nuclei, respectively. For $\hat{Z}<88$, E_f is calculated using the expression given earlier under the fission probability calculation. With A_1 determined, the mass of the other fission fragment is $A_2=\hat{A}-A_1$.

If $\hat{Z}^2/\hat{A}>35$, competition between symmetric and asymmetric fission is allowed, with the asymmetric probability being $P_{asy}= F/(1+F)$ where $F=4870\exp(-0.36\hat{E}^*)$. For asymmetric fission, A_1 is selected from a Gaussian of mean $\bar{A}=140$ and width $\sigma_A=6.5$, and then $A_2=\hat{A}-A_1$.

The charge of the first fragment Z_1 is selected from a Gaussian distribution of mean $\bar{Z}_1$ and width $\sigma_Z=2$, where $Z_1=(\hat{Z}+Z_1'-Z_2')/\ 2$, $Z_i'=C_{15}A_i/(2C_{15}+A_i^{2/3})$, and $C_{15}=65.5$. Then $Z_2=\hat{Z}-Z_1$.

The total kinetic energy of the fission fragment in the center-of-mass E_T', is selected from a Gaussian distribution having mean $\bar{E}_T=0.13\hat{Z}^2/A^{1/3}-11.4$ and width $\sigma_E=0.084E_T'$. These relations are based on evidence of the strong correlation of fission fragment kinetic energies with the Coulomb repulsion parameter $\hat{Z}^2/\hat{A}^{1/3}$ of the fissioning nucleus (e.g., /16/), and data which suggests that the kinetic energies are narrowly distributed about $\bar{E}_T'$. The kinetic energy of each fragment, in the center-of-mass, is $E_1'=A_2E_T'/\hat{A}$, and $E_2'=E_T'-E_1'$. Isotropic emission in the center-of-mass is then assumed to obtain the kinetic energies E_1 and E_2 in the laboratory system.

The excitation energies of the fission fragments is then determined by an energy balance: $E_1^*=(A_1/\hat{A})(\hat{E}^*+B_1+B_2-\hat{B}-E_T')$ and $E_2^*=E_1^*A_2/A_1$, where B denotes binding energies.

3 THIN TARGET CALCULATIONS AND COMPARISONS

In this section, calculations made at KFA using the RAL fission model are compared with results from Alsmiller, et al. /4/ obtained using the ORNL model. All of the comparisons are for protons incident on a thin ^{238}U target. The quantities compared are fission cross sections, neutron production, fragment kinetic energy, and residual mass distributions.

3.1 Fission Cross Section

Fig. 3 shows the fission cross sections calculated by the RAL and ORNL models compared with experimental data. The fission cross sections predicted by the RAL model (Table 3) are about 15-20% lower than for the ORNL model for beam energies below $\sim$1 GeV, and the energy dependence of the cross sections above $\sim$1 GeV appears to be different for the two models. As is evident, the spread of the experimental data is too large to judge the correctness of either model.

Also shown in Fig. 3 are the nonelastic cross sections from the two calculations, which are in agreement, as expected, since both calculations use the same intranuclear cascade model.

3.2 Neutron Production

Figs. 4 and 5 show comparisons of neutron multiplicity from evaporation only (taken to be $\leq$ 12.5 MeV) and over all energies (evaporation plus intranuclear cascade), respectively. For the standard B_0 values used in the two models (B_0=14 for RAL, B_0=10 for ORNL), the RAL model predicts lower neutron emission by about 20-25%. These comparisons also show the sensitivity of neutron production to values assumed for B_0. The variation in neutron production over the range of B_0 parameters suggested as reasonable from present experimental data are about the same as the model differences.

To consider further the influence of B_0, we have calculated the low-energy neutron production spectrum for 1-GeV protons using the RAL model (Fig. 6). The integral neutron production below 12.5 MeV is 20% higher for B_0=8 than for B_0=14. Also, shown in Fig. 6 is the neutron spectrum obtained when high-energy fissioning is neglected.

With fission included, the neutron production is about 8% higher, and there is evidence of some "spectral hardening" for neutron energies above about 2 MeV. Neutron production above this energy is important because this corresponds approximately to the energy threshold for neutron induced fission for ^{238}U. Thus, while the magnitude of spectral hardening introduced by high-energy fission appears to be small, its influence on total neutron production in thick ^{238}U targets can, in principle, be amplified by providing a larger source of neutrons that can cause multiplication via low-energy fissioning. However, this spectral hardening from fission turns out not to have a large influence on the neutron flux from thick targets, as shown later in Section 4.

A summary comparison of the RAL and ORNL high-energy fission models in terms of neutron multiplicities predicted is given in Table 4, from which we conclude: (1) for the standard B_0 values incorporated in the models, the ORNL model predicts about 20% more neutrons, (2) the neutron production is sensitive to the value of B_0 assumed, varying by about 20 % over the range of B_0 values inferred from presently available experimental data, (3) for the same assumed B_0 in each model, the ORNL model still predicts more neutrons than the RAL model, by about 12%, and (4) the effect of high-energy fissioning compared to spallation without fissioning is to increase the neutron production by about 7% (with a somewhat harder spectrum in the energy region from ∿2 to ∿5 MeV.

3.3 Energy of Fission Fragments

There are large differences in energy deposition for spallation collisions with and without high-energy fissioning. If fission takes place, the "local" energy deposition at the collision site is mainly from the kinetic energy of the fission fragments which, as in low-energy fission, is expected to be about 170 MeV per fission. (From non-fissioning spallation collisions, the deposition from heavy short-range secondary particles and residual nuclei is, nominally, only about 20-30 MeV per collision.) Thus, the fission fragment kinetic energies predicted by the high-energy fission model is important in predicting target heating.

A comparison of the (total) fission fragment energies calculated using the RAL and ORNL models is given in Fig. 7, and the agreement is good. As also indicated in Fig. 7, this energy is not sensitive to B_0. This is as expected since the fission fragment energy results mainly from the Coulomb repulsion between fragments. Thus, the fragment energies are not sensitive to few-neutron differences of the fragment masses.

3.4 Residual Mass Distributions

A summary of the mass distribution results for the three beam energies calculated using the RAL model is shown in Fig. 8. The points shown are averages over $\Delta A=5$ intervals and are plotted at the midpoint of the intervals. Representative error bars (one standard deviation) are indicated. The normalization is per non-elastic proton-uranium collision, which can be converted from yields to production cross sections by multiplying by the computed total non-elastic cross section (Table 3).

Note from Fig. 8 that the model predicts a "bump" in production in the mass region between that of the fission products ($A \lesssim 180$) and the mass region of the residual spallation product mass in which fission did not occur ($A \gtrsim 220$);this is discussed in more detail later.

In Figs. 9 and 10 results from the RAL model are compared with ORNL model predictions and measured data. The ORNL calculations are also averaged over $\Delta A=5$ intervals. The normalization of the measured data of Stevenson, et.al /24/ at 300 MeV is taken from the ORNL paper /4/, in which the area under the experimental points in the mass region from 60 to 160 was normalized to be the same as the area under the ORNL calculated histogram in this mass region. (The 2.9 GeV experimental values are the absolute production cross sections given by Friedlander, et.al. /25/, converted to yields using the calculated non-elastic cross section.)

From Figs. 9 and 10, the model predictions and measured data are all in good agreement in the vicinity of the peaks of the fission fragment mass distributions, although the RAL model seems to predict a somewhat wider fission fragment distribution.

As noted earlier, the RAL model predicts three peaks in the mass distribution: The fission fragment peak at $A \sim 110$, the spallation peak at A=238, and an intermediate peak at $A \sim 200$. This intermediate peak apparently results from spallation products which "survive" de-excitation through the mass region of high-fission probability into a lower mass region where further de-excitation by neutron emission is much more likely than fission. To illustrate, we have calculated the mass distributions with and without fission competition for the 1 GeV beam case (Fig. 11). To show the fission probability versus mass number, we have used subroutines of the RAL model to compute the fission probability for various arbitrarily selected isotopes covering the mass range from 175 to 250 (Fig. 12). Thus, while spallation products are produced down to A 160 (for 1 GeV, Fig. 11), and the model allows fission for these low masses, Fig. 12 shows that the fission probability is very small for A $\lesssim$200, accounting for the peak in this region. This intermediate peak in the mass distribution is probably most evident at "medium" beam energies -- i.e., at low beam energies (say, $\sim$ 100 MeV) there is not sufficient excitation energy to produce many nuclei in the lower mass region of low-fission probability, whereas at high beam energies there is sufficient excitation energy that spallation products can be produced with very low masses which overlap with the higher mass fission fragments (as evidenced by the 2.9 GeV results).

Apparently, the ORNL model does not predict an intermediate peak in the mass distribution (Fig. 9), which seems somewhat surprising since the ORNL model neglects fission for nuclei having atomic numbers less than 91.

All of the RAL model results above were computed using a value of 14 for the parameter B_0 in the level density formula, which is the standard value incorporated in the RAL model program. For one case (E_0=1GeV) a calculation using B_0=8 was made for comparison (Fig. 13). Thus, while the value of B_0 used has an important effect on neutron production (Section 3.2), it has little influence on residual mass distributions, as has been pointed out previously, e.g., /4/.

In considering the above mass distributions predicted by the fission models for thin targets, it should be noted that for thick targets the mass yield from fission is often dominated by low-energy fission rather than high-energy fission. As an example, Fig. 14 shows the calculated contributions from low-energy fission and high-energy fission to the residual mass distribution for a thick uranium target bombarded by 1100 MeV protons. (The target configuration here is that of the SNQ reference design /1/, which is a "wheel" 2.5 m in diameter and 10 cm thick, containing target material, water coolant, and aluminium as structural material). In the mass region of the usual asymmetric fission yield peaks for low-energy induced fission (A 90 and A 140), high-energy fission contributes $\sim$25%, with the main contribution of high-energy fission being to produce isotopes in the "valley" between the low-energy peaks.

The general characteristics of these contributions from high-energy and low-energy fission in thick targets is in agreement with measurements made by Russell, et.al. for 800 MeV protons incident on thick uranium targets /26/.

4 THICK TARGET COMPARISONS OF NEUTRON PRODUCTION AND THERMAL FLUXES

To clarify the influence in practical calculational problems of the different "High Energy Fission" (HEF) models and the relationship between the models, a series of calculations was performed and compared with existing experimental data taken from the BNL-Cosmotron experiment (see Refs. 11, 27). This experiment consisted of a H_2O tank 1.83 m diameter and 1.83 m height. Several targets of different sizes and materials, among them depleted uranium and lead, were placed in the center of the tank. The total capture rate in the H_2O tank was measured by foil-activation techniques. For the calculations, we considered a depleted uranium target (0.22 wt% ^{235}U, length 609.6 mm and radius 50.8 mm) and a lead target of the same size. The calculations were done using the HETC, MORSE CG, and SIMPEL spallation computer code system of KFA-IRE as described in References /1/ and /29/. The fractional standard deviation in the Monte Carlo calculations is less than than 1%, unless stated explicitly in the tables.

4.1 Neutron Production Using the HEF Model in the HETC Code

For these calculations, the BNL-Cosmotron setup with incident proton beam energy of 960 MeV was assumed. Calculations of the evaporation part of neutron production spectrum with and without the RAL-HEF model incorporated in HETC were made. In Fig. 15 the two spectra are given. Some spectral hardening in the case of HEF is clearly seen. The total neutron production (see Table 5) including low-energy fission (<15 MeV) is about 6-10% higher using the HEF model. Most of this effect is due to the additional low-energy fission from the harder production spectrum when fission is included.

4.2 Comparison of the RAL-HEF Model Against the ORNL-HEF Model

For these comparisons of the two HEF models at 960 MeV, the calculations were performed first with the "standard" B_0 values of the level-density formula which are incorporated in the models (B_0=10 MeV for ORNL, B_0=14 MeV for RAL). Secondly, the RAL model was run with two additional values of B_0: 8 MeV and 10 MeV. The use of these standard B_0 values give differences of about 20 % in neutron production and capture rates. If we use B_0 of 10 MeV for both models, the difference is reduced to about 10% (see Table 6). The neutron production spectra are very similar (Fig. 16). The effect of different B_0 values for the RAL-HEF model is shown in Table 7 and illustrated in Fig. 17

4.3 Calculated Neutron Captures in H_2O Compared with BNL-Cosmotron Experimental Results

Table 8 compares calculated results for neutron captures in water with the Cosmotron data for proton beam energies of 540, 960, and 1470 MeV. For the "standard" B_0 values used in the models, the ORNL model gives better agreement with experiment at 540 MeV, the RAL model gives better agreement at 1470 MeV, and both models give predictions within about ±10% of the measured data at 960 MeV. With the same B_0=10 MeV for both models, the calculations at 960 MeV are within ± 4% of the experiment, and for a B_0=8 MeV the RAL model matches the experimental value exactly at this beam energy.

The calculations of Alsmiller, et.al. /11/ using the ORNL model did not take into account self-shielding corrections for the uranium cross sections used in the low-energy MORSE code transport calculations. Calculations at KFA-IRE were made using the ORNL model and a set of cross sections for MORSE with self-shielding, but, as indicated in Table 8, the difference due to this effect is small.

Some more detailed information on the RAL model results for neutron production spectra and neutron captures is given in Fig. 18 and Table 9 for the depleted uranium target and different beam energies. Comparisons for different target materials are given in Fig. 19 and Table 10.

4.4 Comparisons of Thermal Neutron Flux in Water Moderator

Here we compare the thermal neutron flux produced in the water moderator of the cosmotron experiment setup for different model assumptions. All of the high-energy fission calculations for these results were made using the RAL model.

Spatial Dependence

As a general indication of the thermal flux spatial distribution produced, Figs. 20 and 21 show three-dimensional plots for uranium and lead targets for an incident proton beam energy of 960 MeV. It is obvious that the flux distribution is more concentrated for the uranium target, mainly because of its higher density.

Fig. 22 compares the radial distribution of the thermal flux at the depth intervals where the flux is maximum, and Fig. 23 compares the depth distribution where the flux is a maximum radially, both for a 540 MeV proton beam energy. Figs. 24-27 show similar plots for beam energies of 960 and 1470 MeV.

Figs. 28-32 compare radial distributions of the thermal flux from the present calculations, previous calculations of Coleman and Alsmiller /28/ using an earlier version of the

HETC code and neglecting high-energy fission, and the data of Fraser, et.al. from the Cosmotron experiments /27/. The agreement between the two calculations is quite good, and the calculations and measurements are in good agreement for the uranium target (Fig. 32), but the calculations over-predict somewhat the flux for the lead target.

Peak Fluxes

Table 11 summarizes the peak thermal flux values in the water moderator for the various calculated cases, with the normalization given both per incident proton/s and per milliampere of incident beam current. The cases denoted "no RAL" were calculated using the standard evaporation model of the HETC code, which does not include fission and uses B_0=8 MeV.

A comparison of the ratio of peak thermal fluxes for uranium and lead targets is summarized in Table 12 for various model assumptions. Note that this ratio can vary substantially (from 1.7 to 2.5) with model assumptions. As indicated in Table 12, when the RAL model with its standard B_0 value of 14 is used for both lead and uranium, the peak flux ratio is 1.9-2.2; whereas if the standard HETC evaporation model is used for lead, the ratio is 1.7-1.8. The fission probability for lead is quite small, so these differences are due to the difference in B_0 values used for the lead calculation rather than high-energy fission effects for lead. Note from the last line of Table 12 that if the standard evaporation model in HETC is used for both lead and uranium (as was done, for example, in previous calculations by Coleman and Alsmiller /28/), the U/Pb flux ratio is 1.9, which is in good agreement with the ratio value obtained with fission for uranium included.

Some additional peak flux ratios, all for 960 MeV beam, are given in Table 13. Note from the first two lines of Table 13 that the lead results are much more sensitive to the assumed value for B_0 than for the uranium target. Note also (line 3) that high-energy fission has a very small effect on the peak thermal flux. Finally, from the last line of Table 13, a natural uranium target provides about a 20% increase in the time-averaged peak thermal flux over a depleted uranium target.

Fig. 33 shows the dependence of the peak thermal flux for depleted uranium and lead targets upon the incident proton beam energy. While the uranium target produces a peak flux about two times the lead target over the entire proton beam energy range, the magnitude of the peak neutron flux begins to increase less than linearly with proton energy above about 1 GeV. This is because at the higher beam energies the cascade becomes more spread out spatially and because of the larger fraction of beam energy beginning to be converted to pion production rather than neutron production.

4.5 Energy Deposition

Table 14 is shown as an example to indicate the contribution of high-energy fission to the energy deposition produced in the target. For this case of the Cosmotron experimental set-up, a depleted uranium target, and 960 MeV proton beam, the fission fragments from high-energy fission deposit about 300 MeV per proton to the energy deposition. The contribution to the energy deposition from low-energy (<15 MeV) neutrons, which is primarily from fission, has not been calculated here for this case, but based on previous calculations /1/, the low-energy neutrons are expected to contribute $\sim$ 1 GeV/proton to the deposition. Therefore, the high-energy fission contributes 15-25% to the total deposition.

It might be noted that the calculations of Coleman and Alsmiller /28/ for the Cosmotron experiments did not include the energy deposition from high-energy fission, so the total energy deposition values given in /28/ for uranium targets are expected to be too low by ∿20%.

5 CONCLUSIONS

The calculations here have quantified the differences in neutron production predicted by the high-energy fission models developed at the Rutherford Appleton Laboratory and the Oak Ridge National Laboratory. For thin U-238 targets and proton beams in the 0.3-3.0 GeV energy range, the ORNL model predicts about 25% more neutrons than the RAL model (Table 4). This difference is comparable to the spread in the present experimental data for thin target neutron production (Fig. 4), and it is not possible to judge the correctness of one model over the other. The differences between the two model predictions can be reduced by adjusting the assumed values used for the B_0 parameter in the evaporation model level density formula.

The accuracy of the high-energy fission models for spallation neutron source applications has been checked by making comparisons with the measurements of Fraser, et.al. for proton beams incident on a long, cylindrical uranium target surrounded by a large water moderator. Using the total neutron captures in the water as a basis, both fission models give predictions within about +20% of the measurements over the proton energy range from about 500 to 1500 MeV (Table 8). The model agreement with experiment varies with beam energy, with the ORNL model somewhat better at low beam energies and the RAL model better at high energies. These comparisons show that agreement with the Fraser, et al. data below 1 GeV is improved for the RAL model if a value for B_0 is used that is less than the standard values of 14 incorporated in the model. Thus, in the absence of additional data for guidance, we suggest that the RAL be applied with B_0=8 for beams $\sim$1 GeV and B_0 = 14 at higher energies.

Calculations made for uranium targets with and without high-energy fission included (but with the same value for B_0) show that fission has only a small effect (<10%) on neutron production and thermal neutron flux. For example, for 1 GeV proton beams, the thin-target neutron production is 7% higher with fission (Table 4), the thick target neutron production is 2% higher (Table 5), neutron captures in the moderator is 6% higher (Table 5) and the peak thermal flux in the moderator is 4% higher (Table 13). The neutron spectrum from proton collisions with uranium nuclei is harder if fission occurs (Fig. 6), and the thick-target neutron production spectrum is noticeably harder with fission (Fig. 15), but the magnitude of these spectral differences are small and not of practical importance in predicting the neutron flux output from spallation sources. It is, however, important to include high-energy fission for predictions of residual mass distributions (Figs. 11 and 14) and target energy deposition (Table 14).

The RAL and ORNL fission models have also been compared for residual mass distributions. Where measured data are available for comparison, both models are in general agreement with the measurements (Figs. 9 and 10). Therefore, either fission model is expected to be adequate for overall estimates of the induced radioactivity associated with spallation neutron sources, particularly since much of the radioactivity is due to low-energy fission rather than high-energy fission (Fig. 14). However, for specific residual nuclei, the two models may predict very different magnitudes, especially in the mass region from $A\sim160$ to $A\sim220$ (Fig. 9).

The calculations here have shown that the B_0 parameter has an important influence on the model predictions of neutron production, particularly for lead targets. Both the RAL and ORNL models assume, effectively, that the level density is linear with the mass number during the nuclear de-excitation chain - i.e., $a \sim A/B_0$ MeV^{-1}. From different experiments on nuclear level spacing, it is observed that the level density is much different for magic nuclei, such as lead, than for mid-shell nuclei. For this reason, an option has recently been added to the version of the HETC code used at KFA-IRE to incorporate a method for specifying a variable level density parameter which is non-linear with A and takes into account shell effects /29/.

6 ACKNOWLEDGEMENT

We are very grateful to F. Atchison for his assistance in providing us the programming for the Rutherford Appleton Laboratory fission model.

7 REFERENCES

1. T.W. Armstrong, P. Cloth, D. Filges, and R.D. Neef
Theoretical Target Physics Studies for the SNQ
Spallation Neutron Source
KFA-Jülich, Germany, Jül-Spez-120, Juli 1981

2. T.W. Armstrong and K.C. Chandler
HETC - A High-Energy Transport Code
Nucl. Sci. and Engr. 49, 110 1972

3. F. Atchison
Spallation and Fission in Heavy Metal Nuclei Under
Medium Energy Proton Bombardment
Meeting on Targets for Neutron Beam Spallation
Sources, G. Bauer (Editor), KFA-Jülich, Germany, 11-12 June 1979,
Jül-conf-34, January 1980

4. F.S. Alsmiller, R.G. Alsmiller Jr., T.A. Gabriel,
R.A. Lillie, and J. Barish
A Phenomenological Model for Particle Production from the
Collision of Nucleons and Pions with Fissile Elements at
Medium Energies
Oak Ridge National Laboratory, ORNL-TM-7528, March 1981

5. H. Takahashi,
Fission Reaction in High-Energy Cascade
Proc. of Symp. on Neutron Cross Sections 10-50 MeV,
Brookhaven National Laboratory, 12-14 May 1980

6. Y. Nakahara
Studies on High-Energy Spallation and Fission Reactions
Proc. of 4th Meeting of International Collaboration on
Advanced Neutron Sources (ICANS-IV), KEK National Laboratory
for High-Energy Physics, Tsukuba, Japan, 20-24 October 1980

7. W.A. Coleman and T.W. Armstrong
NMTC - A Nucleon-Meson Transport Code
Nucl. Sci. and Engr. 43, 353 (1971)

8. V.S. Barashenkov, V.M. Mal'tsev, and V.D. Toneev
Calculation of Fast Particle Induced Fission
Dubna Report JINR P-1970, 1965

9. P. Fong
Statistical Theory of Nuclear Fission
Gordon and Beach Science Publishers, New York, 1969

10. I. Dostrovsky, P. Rabinowitz, and R. Bivins
Monte Carlo Calculations of High-Energy Nuclear Interactions
I Systematics of Nuclear Evaporation
Phys. Rev. 111, 1659 (1958)

11. R.G. Alsmiller Jr., T.A. Gabriel, J. Barish, and F.S. Alsmiller
Neutron Production by Medium Energy (< 1.5 GeV) Protons in Thick
Uranium Targets
Oak Ridge National Laboratory, ORNL-TM-7527, January 1981

12. G.J. Fraser, et al.
Neutron Production in Thick Targets of Lead, Thorium and
Uranium Bombarded by 480 MeV Protons
Proc. of Symp. on Neutron Cross Section from 10-50 MeV,
Brookhaven National Laboratoy, 12-14 May 1980

13. G.J. Russell, et al.
Measurements of Spallation Target-Moderator-Reflector Neutronics
at the Weapons Neutron Research Facility
Proc. of 4th Meeting of International Collaboration on
Advanced Neutron Sources (ICANS-IV), KEK National Laboratory
for High-Energy Physics, Tsukuba, Japan 20-24 October 1980

14. R.G. Vasil'kov, et al.
Atomnaya Energiya 44, 329 (1978)

15. V.S. Barashenkov, V.M. Mal'tsev, and V.D. Toneev
Interaction of Fast Protons with Heavy Nuclei
JINR-R-1969, Dubna (1965)

16. Earl K. Hyde
The Nuclear Properties of the Heavy Elements
Vol. III: Fission Phenomena
Dover Publications, Inc., New York, 1971

17. A. Garvon, H.C. Britt, E. Konecny, J. Weber, and J.B. Wilhelmy
Γ_n/Γ_f for Actinide Nuclei using (^{3}He,df) and (^{3}He,tf) Reactions
Phys. Rev. C 13, 2374 (1976)

18. R. Vandenbosch and J.R. Huizenza
Nuclear Fission, Academic Press, New York, 1973

19. V.S. Barashenkov, A.S. Iljnov, and V.D. Toneev
Fission and Decay of Excited Nuclei
Nuclear Physics A206, 131 (1973)

20. E.F. Neuzil and A.W. Fairhall
Fission Product Yields in Helium Ion Induced Fission of
Au-197, Pb-204 and Pb-206 Targets
Phys. Rev. 129, 2705 (1963)

21. Seaborg and Vandenbosch
Phys. Rev. 88, 507 (1952) and Phys. Rev. 110, 507 (1958)

22. V.S. Barashenkov and S. Ju. Shmakov
Nuclear Fission Induced by High-Energy Protons
JINR, Dubna (1979)

23. R.L. Hahn and H.W. Bertini
Calculations of Spallation-Fission Competition in the Reaction of Protons with Heavy Elements at Energies < 3 GeV
Phys. Rev. C6, 660 (1972)

24. P.C. Stevenson, et al.
Further Radiochemical Studies of the High-Energy Fission Products
Phys. Rev. 111, 886 (1958)

25. G. Friedlander
Fission of Heavy Elements by High-Energy Protons, in Physics and Chemistry of Fission
International Atomic Energy Agency, Vienna 1965

26. G.J. Russell, J.S. Gilmore, H. Robinson and R.E. Prael
Fertile-To-Fissile and Fission Measurements for Depleted Uranium Targets Bombarded by 800 MeV Protons
Los Alamos National Laboratory, LA-UR-81-1815, June 1981

27. J.S. Fraser, R.E. Green, J.W. Hilborn, J.C.D. Milton, W.A. Gibson, E.E. Cross, and A. Zucker
Neutron Production in Thick Targets Bombarded by High-Energy Protons
Phys. in Canada 21, 17, (1965)

28. W.A. Coleman and R.G. Alsmiller Jr.
Thermal-Neutron Flux Generation by High-Energy Protons
Nucl. Sci. Engr. 34, 104 (1963)

29. P. Cloth, D. Filges, G. Sterzenbach, T.W. Armstrong, B.L. Colborn
The KFA-Version of the High-Energy Transport Code HETC and the generalized Evaluation Code SIMPEL
KFA Jülich Report Jül-Spez-196, (1983)

8 APPENDIX A
FIGURES

Consider as 4-step process:

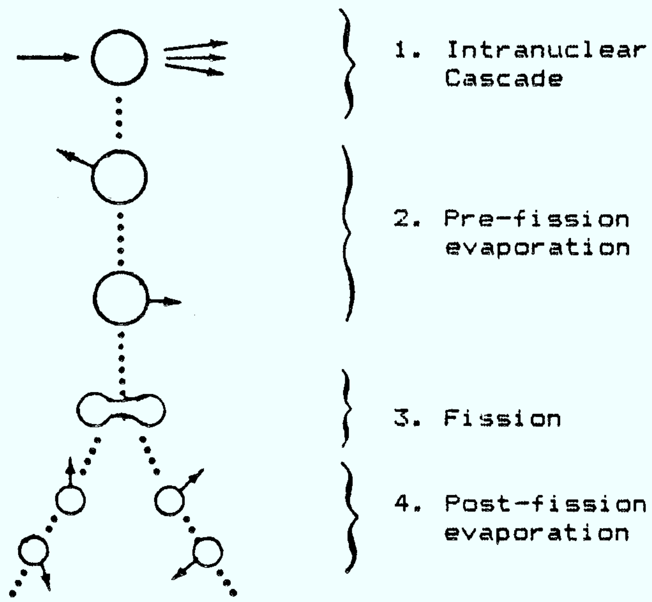

Must determine:

a. Fission probability at each step of de-excitation:

$P_f(E^*, A, Z)$

b. Parameters for fission products at fission:

E_1^*, E_2^* : excitation energies
E_1, E_2 : kinetic energies
Z_1, Z_2 : charge numbers
A_1, A_2 : mass numbers

Figure 1: High-Energy Fission Model

1. Basic Approaches

- RAL
  empirical formulas used as far as possible

- ORNL
  heavy reliance on empirically derived constants
  Note: Fission neglected for subactinides ($Z < 91$)

- BNL
  close simulation of Fong's statistical model formulas, minimum reliance on experimental data

- JAERI
  similar to RAL approach, but different in detail

2. B_0 Values Used in Standard Versions

Model	B_0
RAL	14
ORNL	10
BNL	8
JAERI	8

Figure 2: Features of Different High-Energy Fission Models

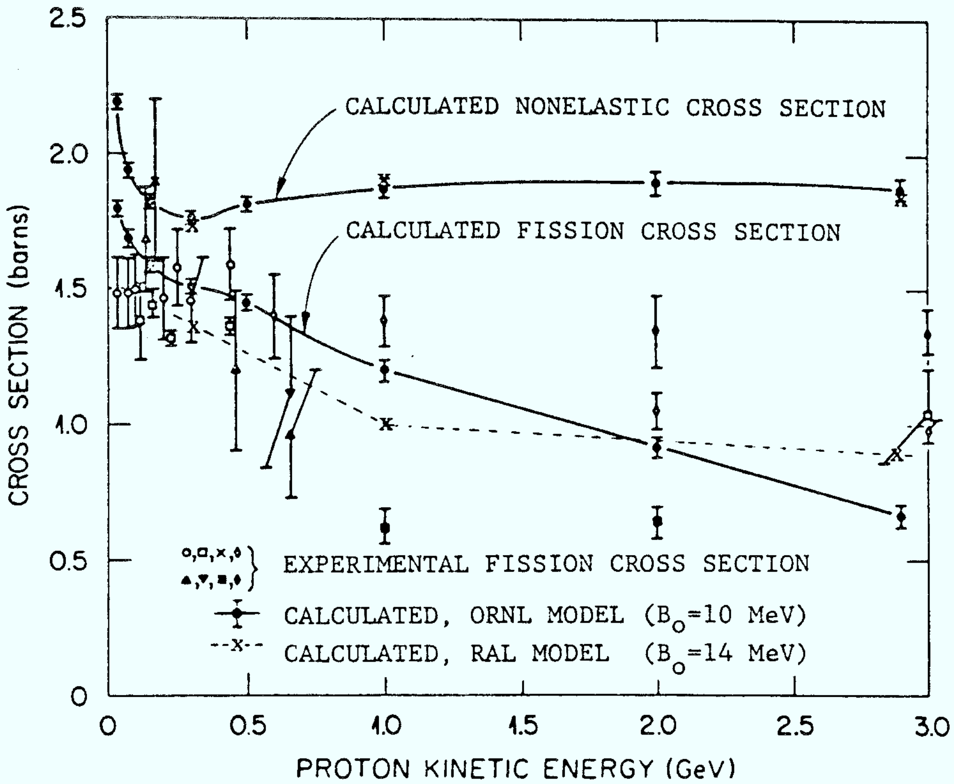

Figure 3: Comparison of calculated cross sections using the RAL and ORNL fission models for the case of protons incident on thin U-238 target. References for experimental data given in /4/

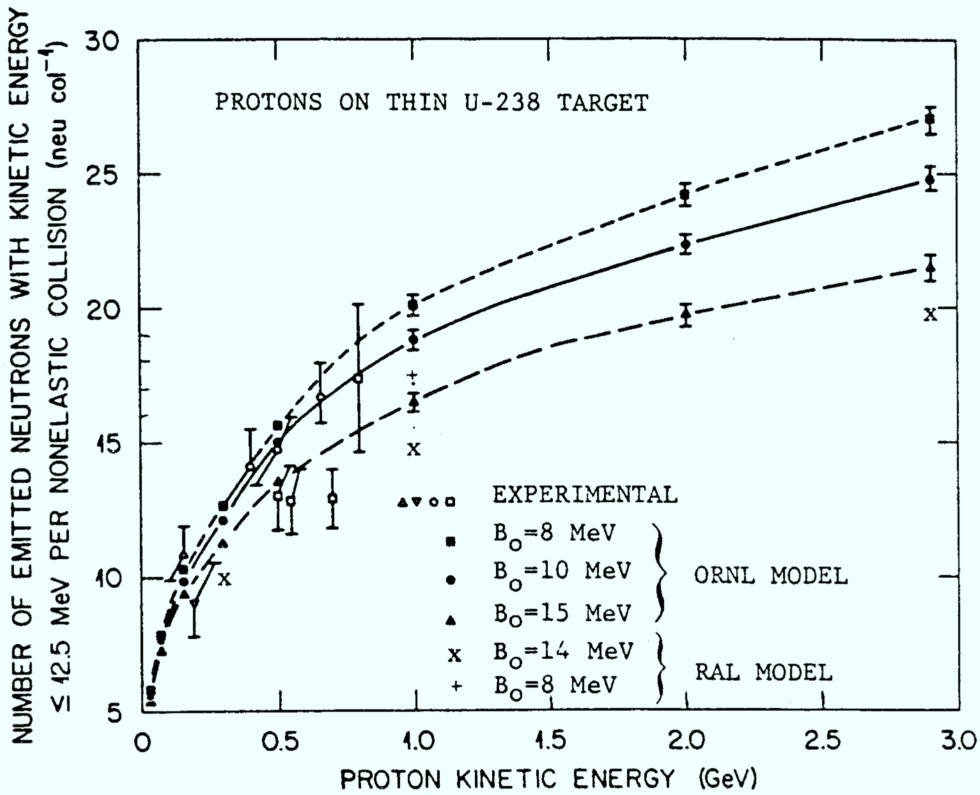

Figure 4: Comparison of RAL and ORNL fission model predictions for neutron production below 12.5 MeV. References for experimental data given in /4/

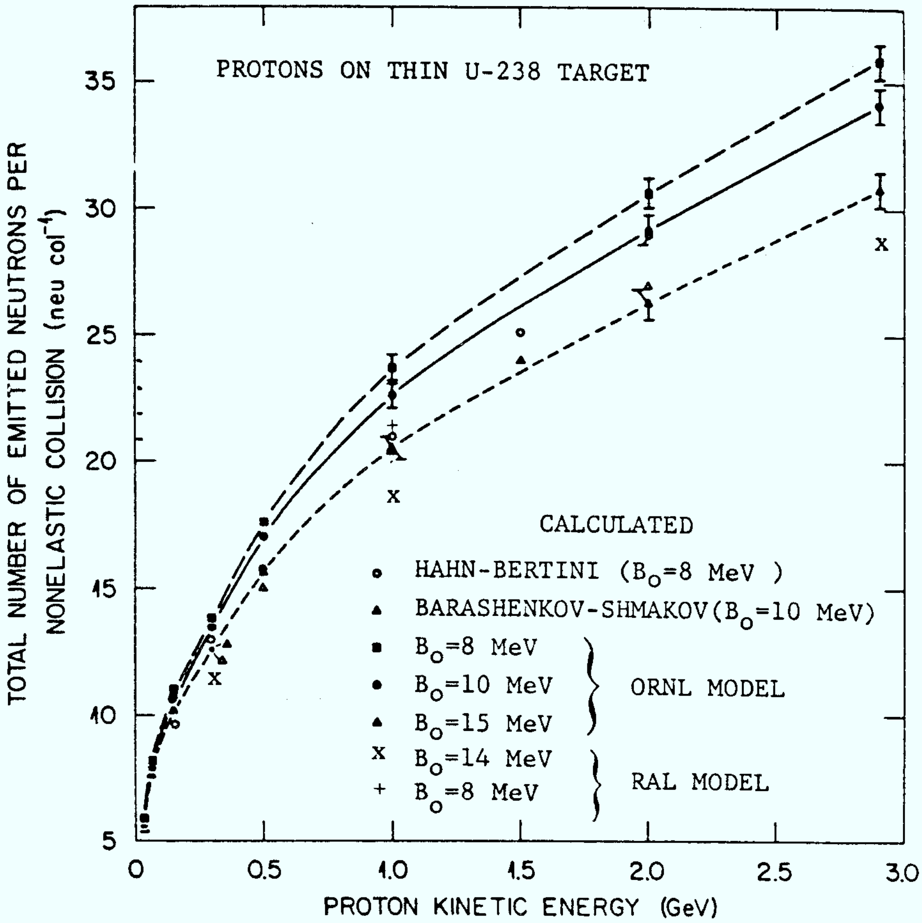

Figure 5: Comparison of total (evaporation plus cascade) neutron production predicted using RAL and ORNL high-energy fission models. Also shown are the results of Barashenkov and Shmakov using the Dubna fission model /22/. The calculations of Hahn and Bertini were made neglecting fission /23/

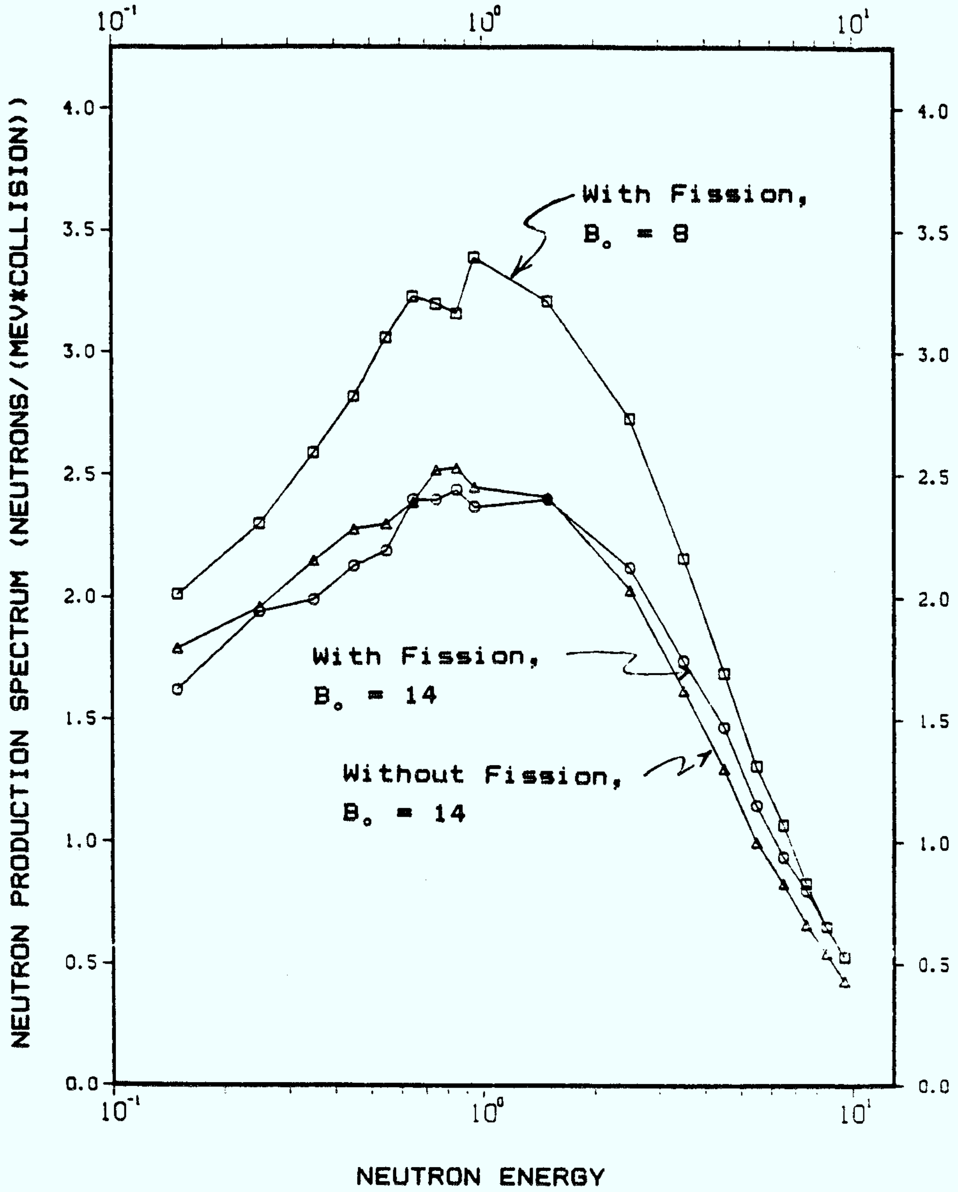

Figure 6: Low-energy neutron production spectrum calculated using RAL fission model, 1-GeV proton beam on thin U-238 target

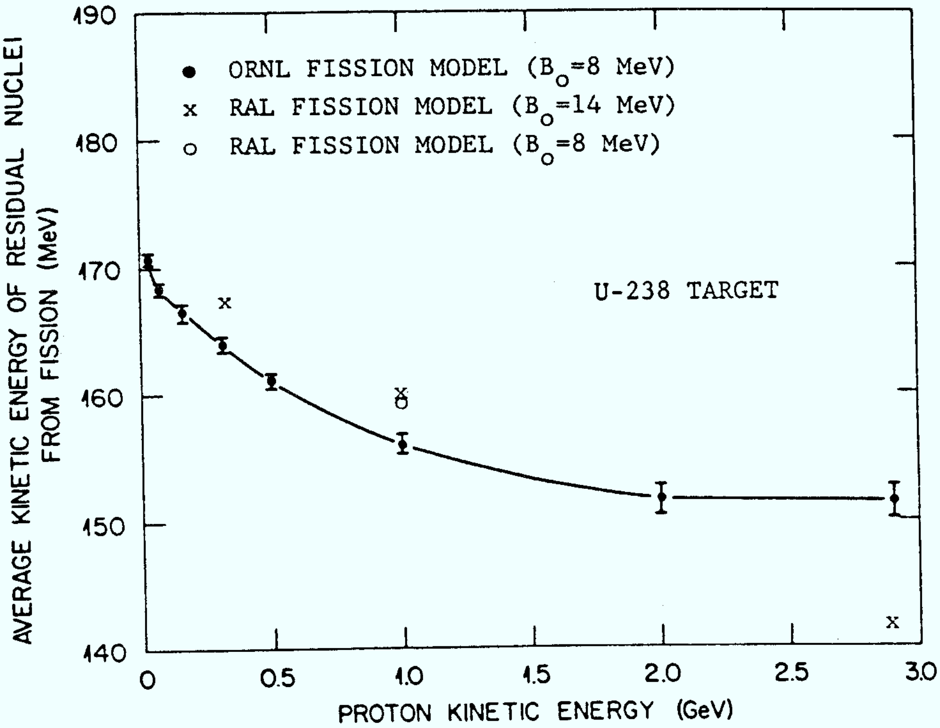

Figure 7: Comparison of fission fragment energies predicted by the RAL and ORNL fission models for protons incident on thin U-238 target

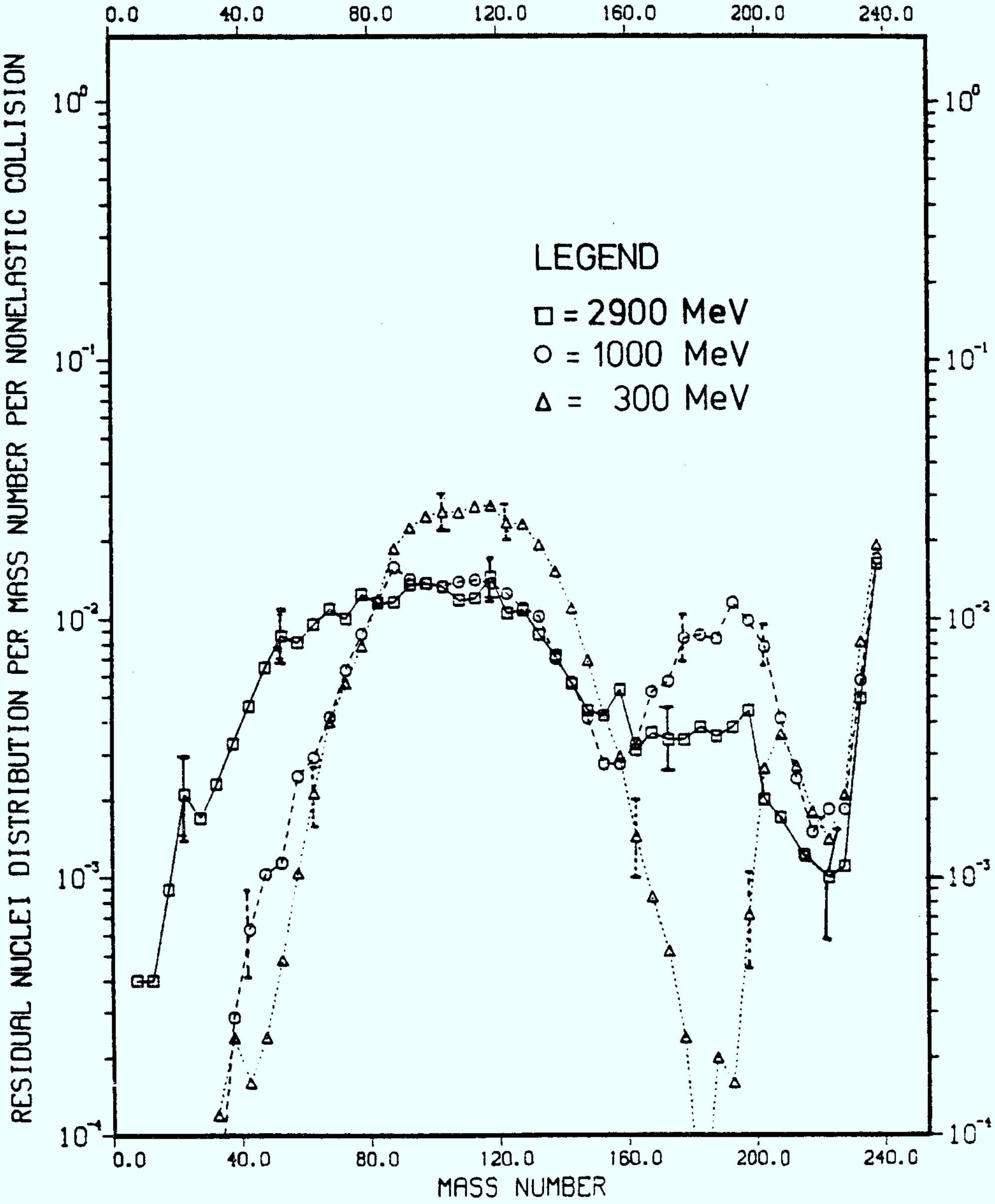

Figure 8: Mass distributions predicted by RAL high-energy fission model for 300, 1000, and 2900 MeV protons on thin U-238 target

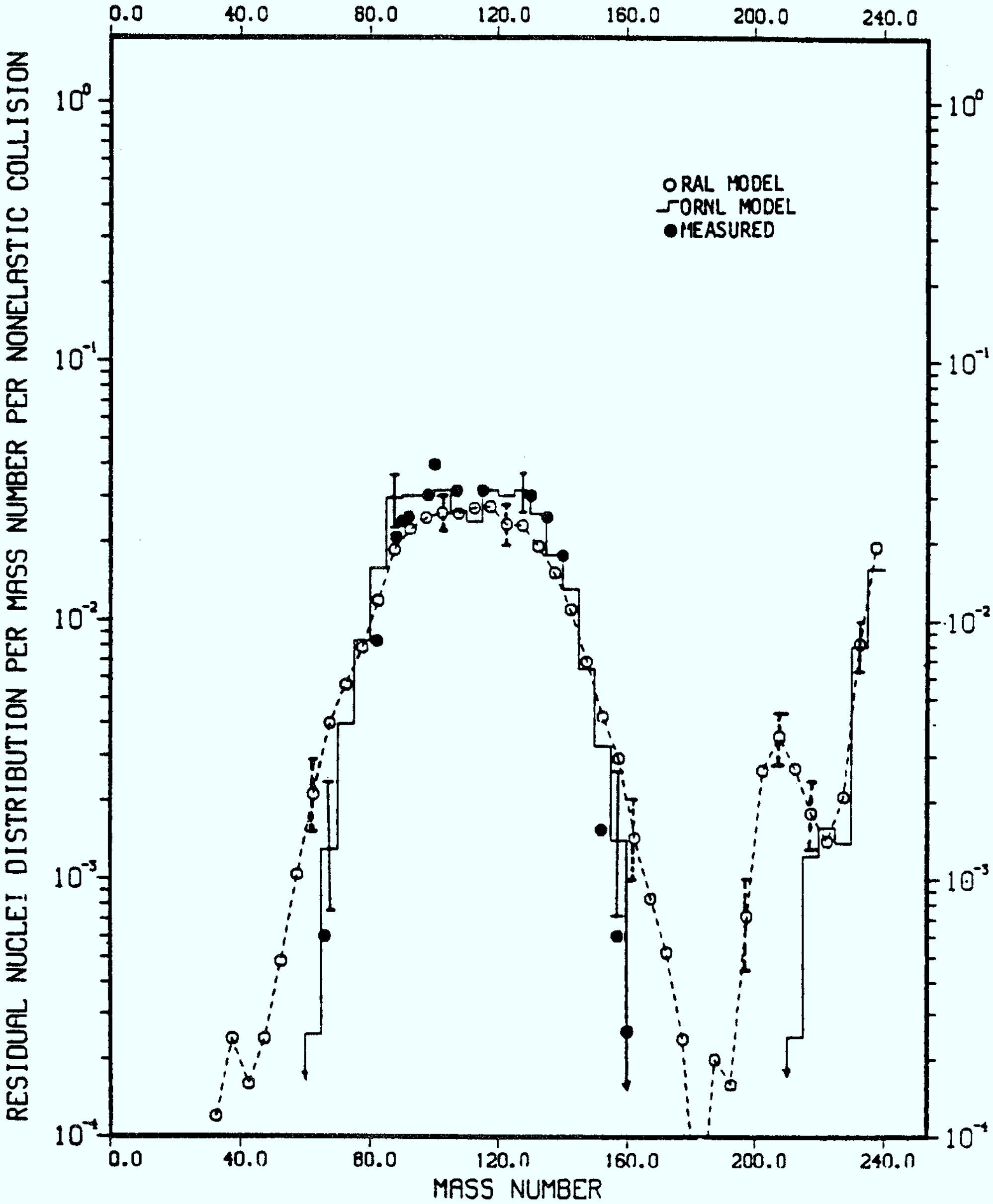

Figure 9: Comparison of mass distributions computed using RAL model, from ORNL model calculations /4/, and from measurements of Stevenson, et al. /24/ for 300 MeV protons on thin U-238 target

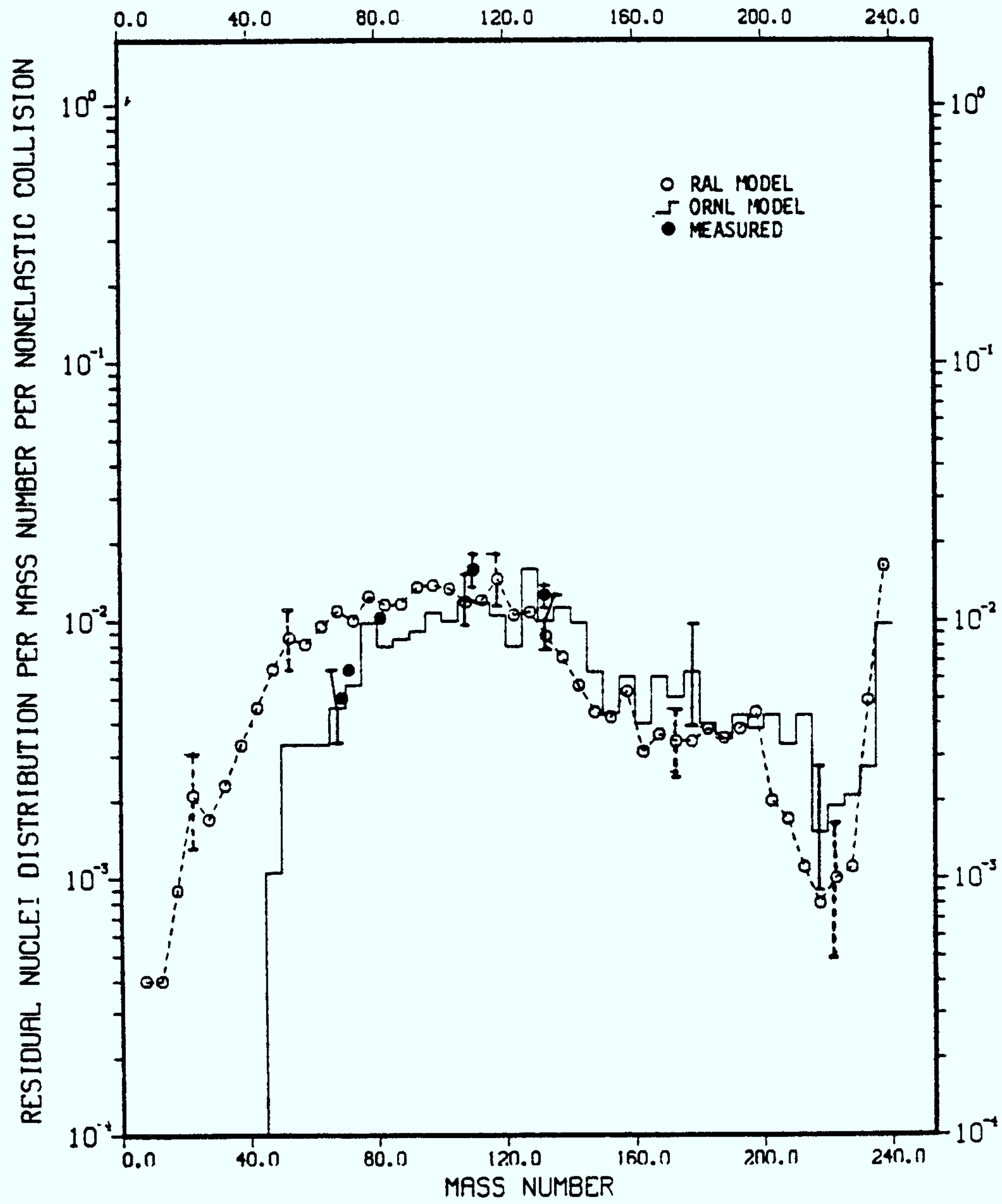

Figure 10: Compari3on of .iass distributions computed using RAL moc̈el, from ORNL model calculations /4/, and from measurements of Friedlander, et al. /25/ for 2.00 MeV protons on thin U-238 target

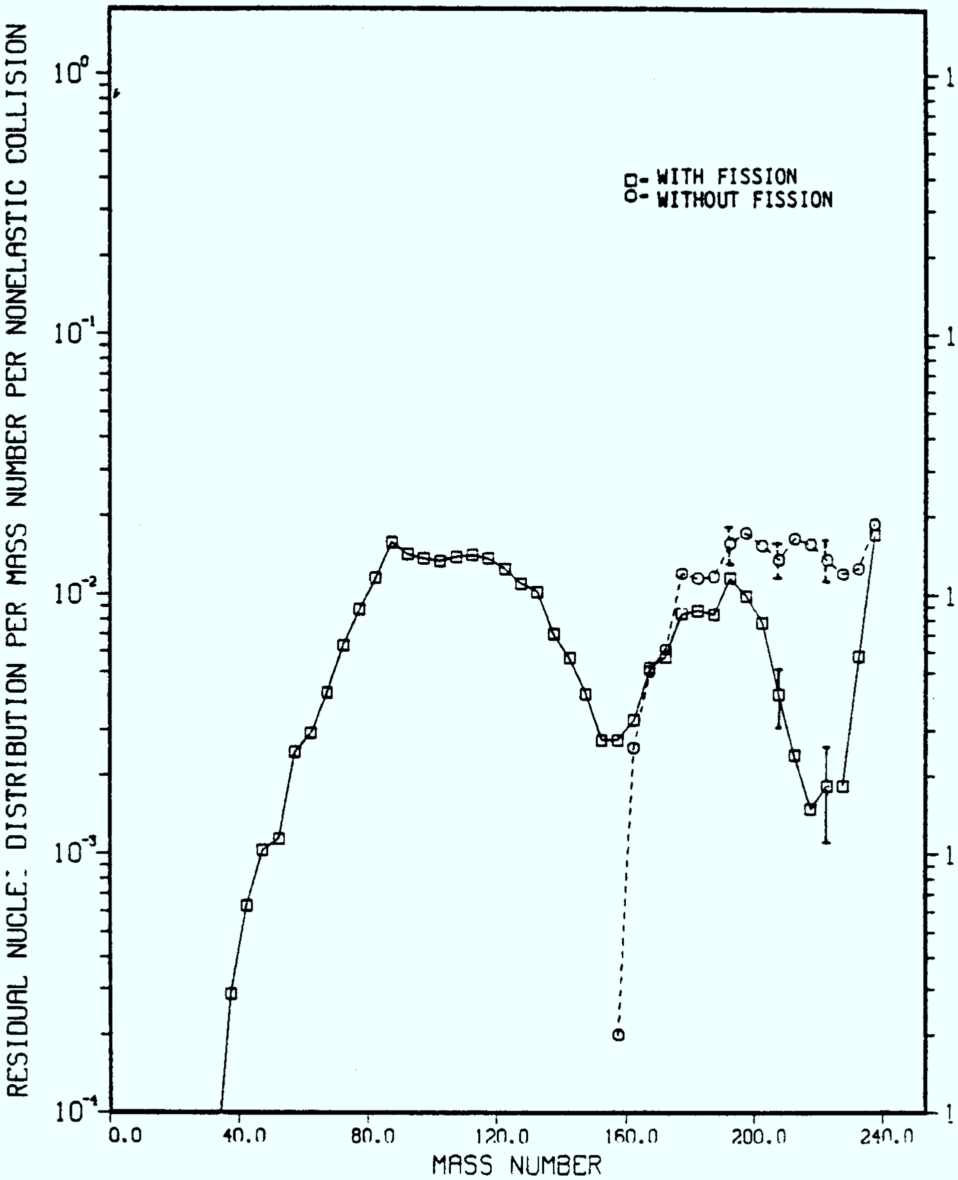

Figure 11: Comparison of mass distributions with and without high-energy fission taken into account for 1-GeV protons on U-238

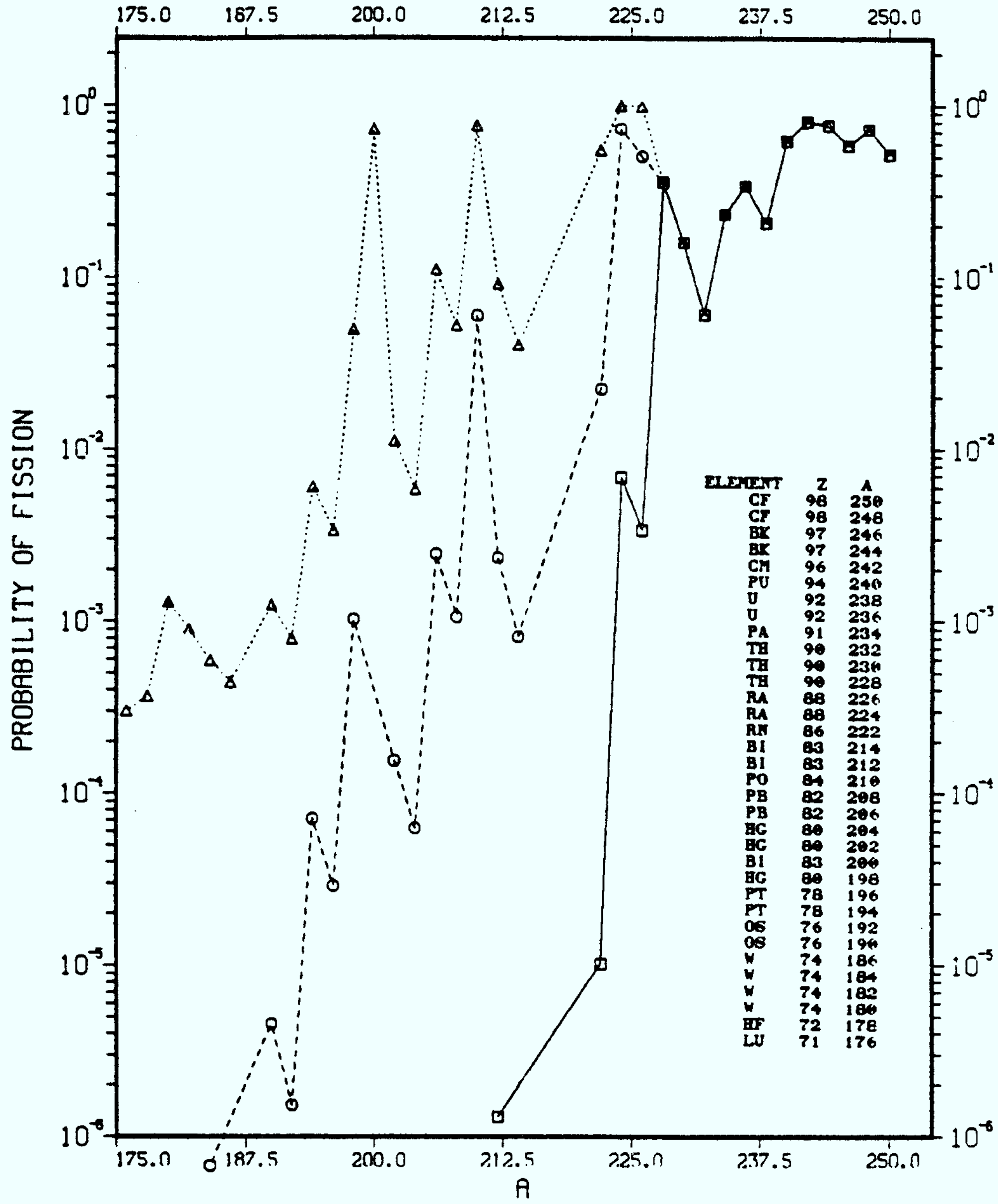

Figure 12: Probability of fission computed using RAL model for various isotopes arbitrarily selected over the range from A=175 - 250. The top, middle, and bottom curves are for assumed excitation energies of 100, 50, and 20 MeV, respectively. (The model assumes that the fission probability is constant for excitation energies above 6 MeV for isotopes having Z above 90)

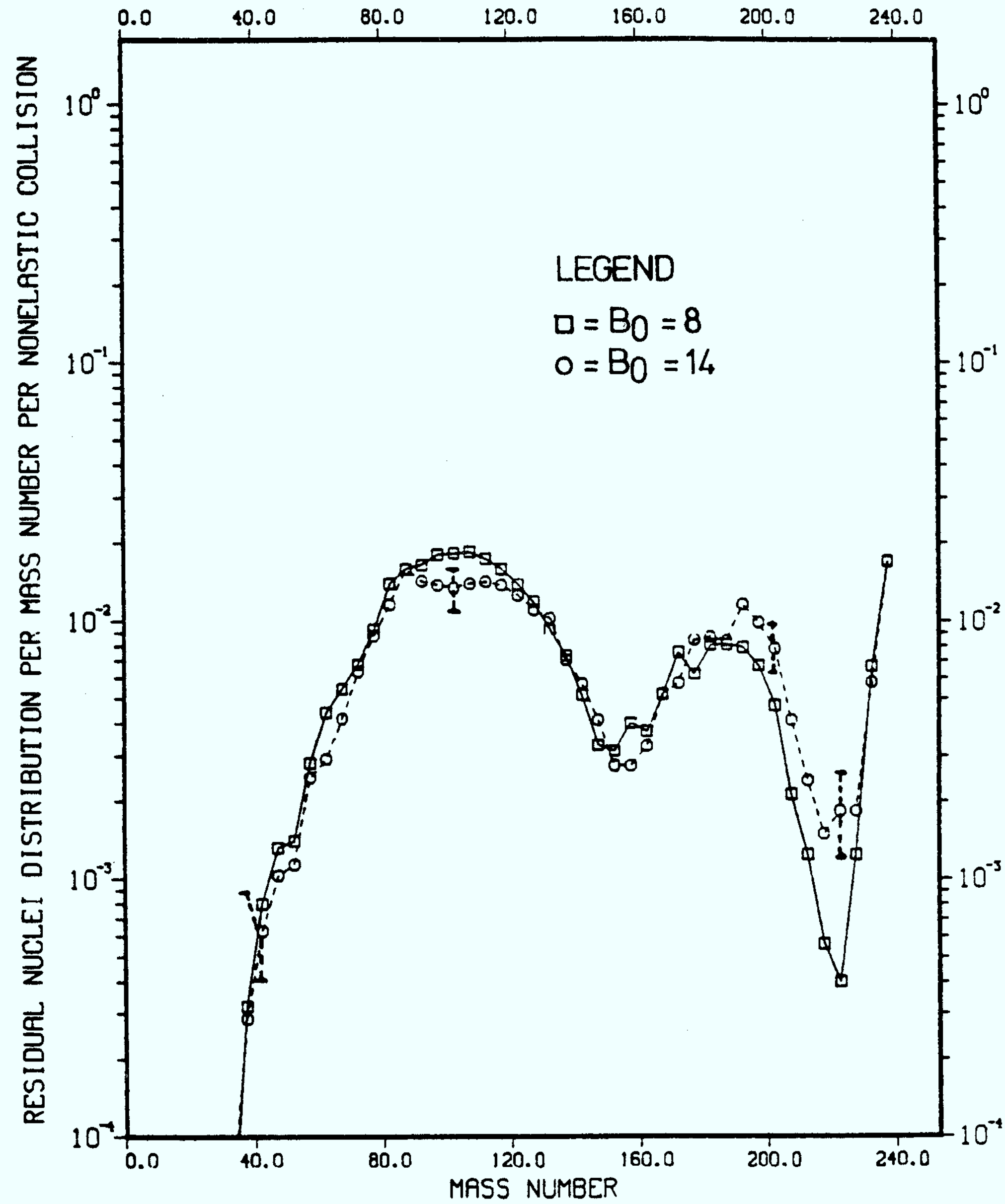

Figure 13: Comparison of mass distributions predicted by the RAL model for level density parameter values B_0=8 and B_0=14 for 1 GeV protons on U-238

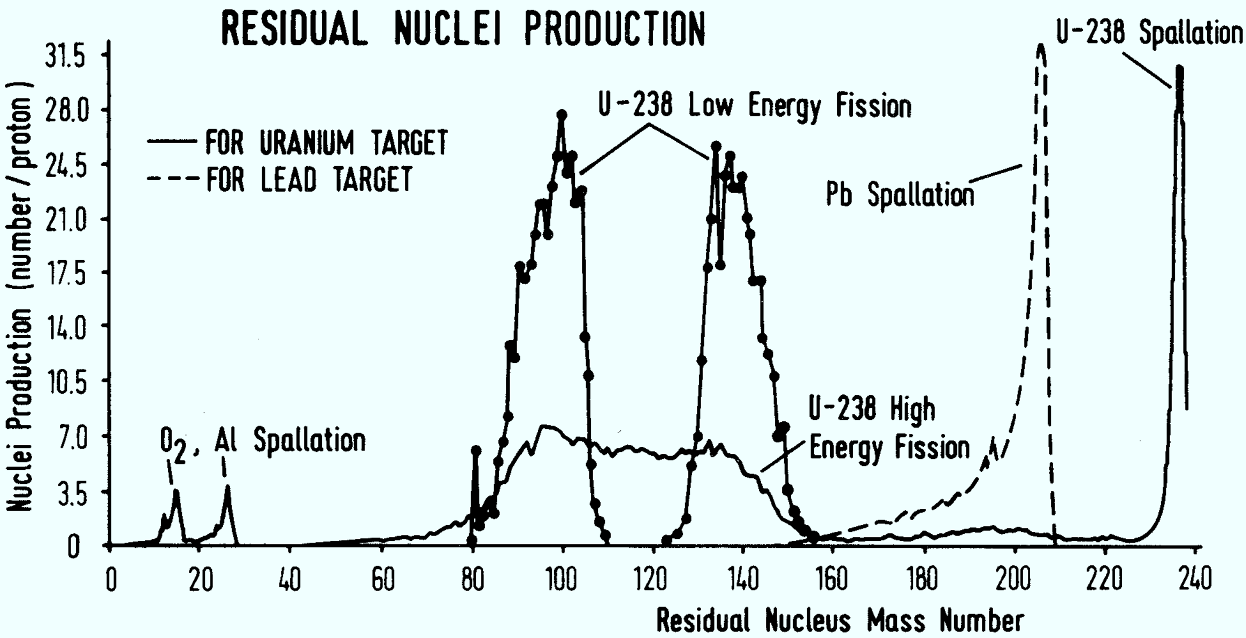

Figure 14: Mass distributions of isotopes produced for Pb and for U-238 as target materials, SNQ reference design target geometry, 1100-MeV proton beam /1/

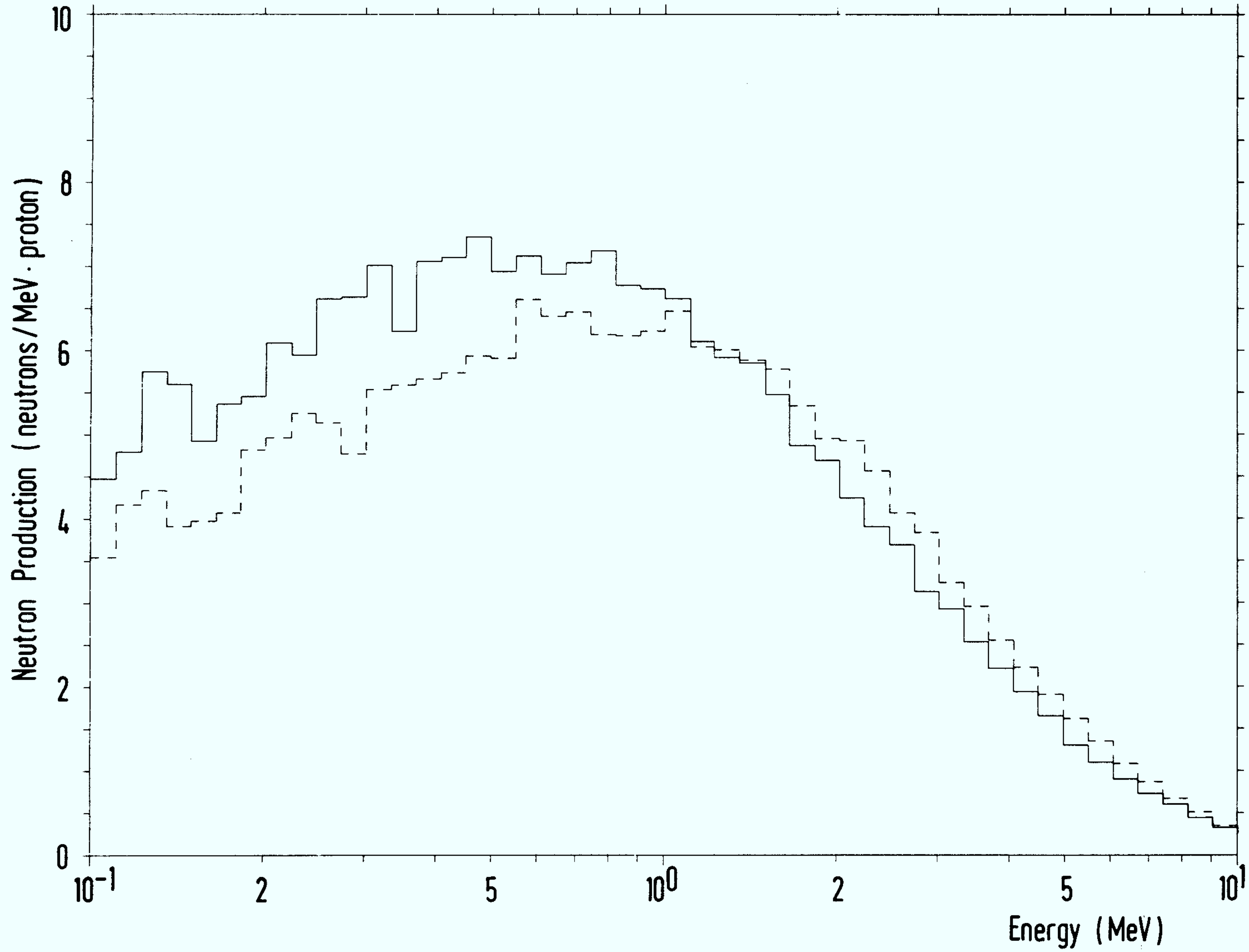

Figure 15: Evaporation neutrons with (dashed curve) and without (solid curve) RAL-HEF model (B_0=8 MeV, proton-beam energy 960 MeV, target material depleted uranium)

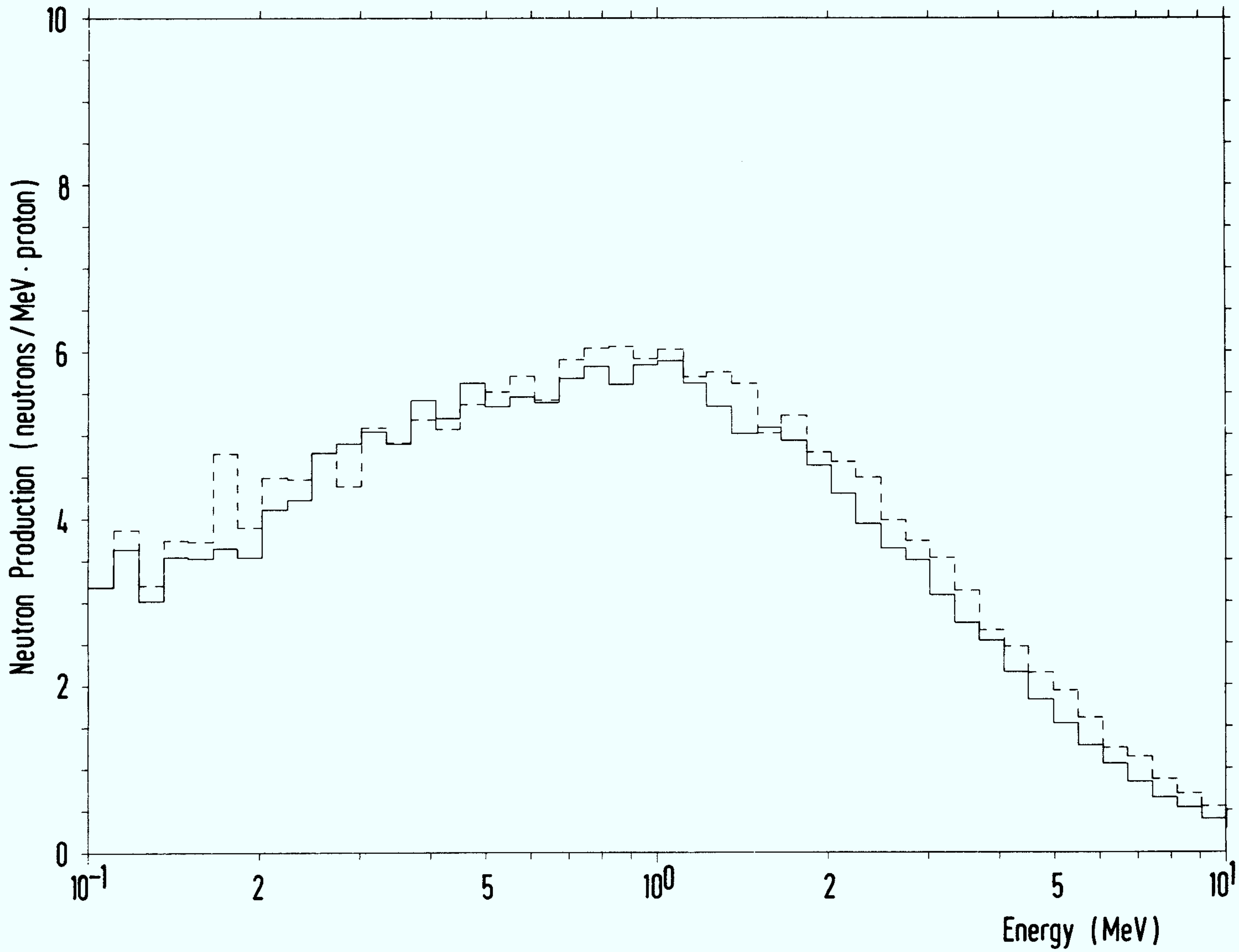

Figure 16: Evaporation neutrons with RAL-HEF model (solid curve) and ORNL-HEF model (dashed curve) (B_0=10 MeV, proton beam energy 960 MeV, target material depleted uranium)

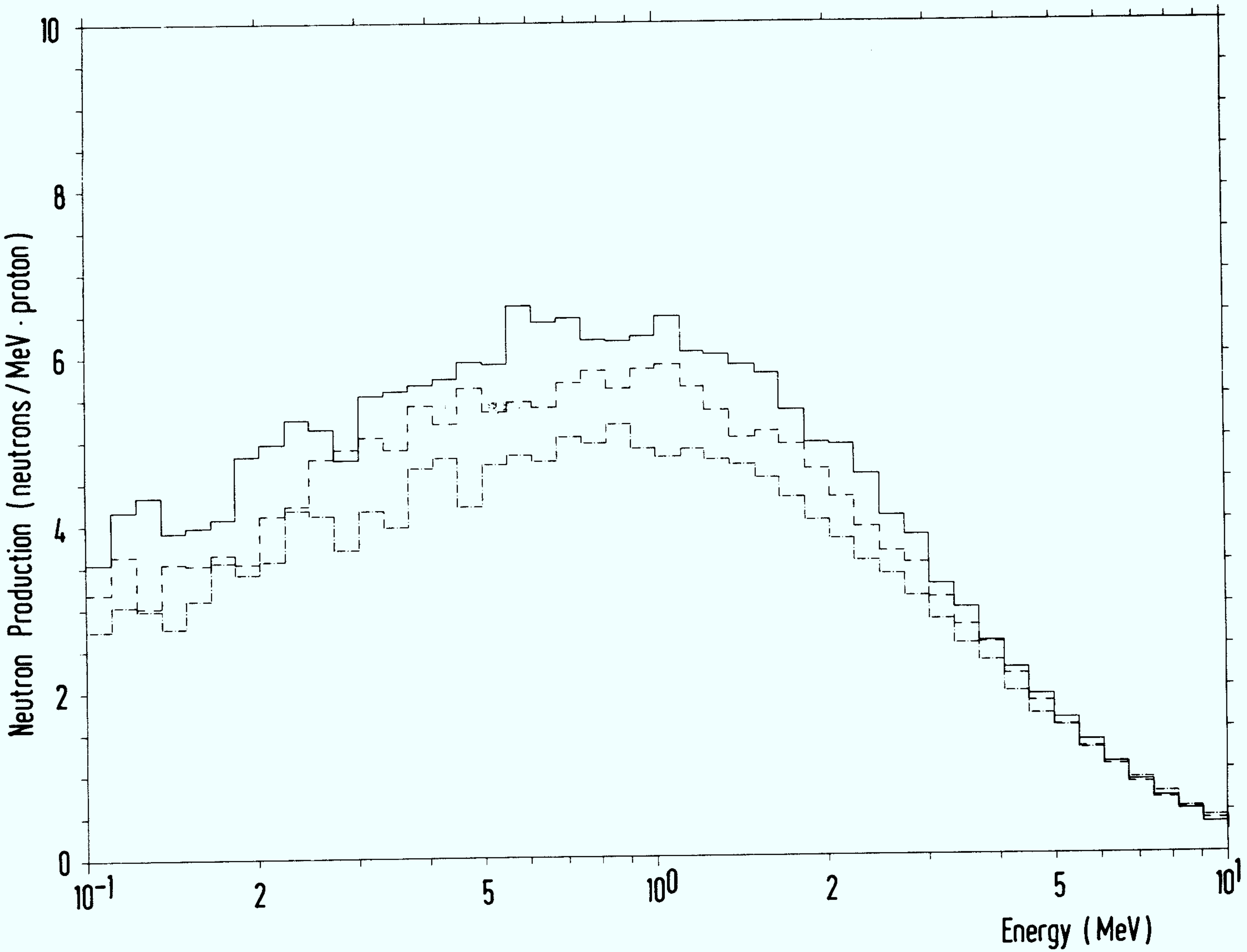

Figure 17: Evaporation neutrons with RAL-HEF model at B_0=8 MeV (solid curve), B_0=10 MeV (dashed curve) and B_0=14 MeV (dashed-dotted curve) (proton beam energy 960 MeV, target material depleted uranium)

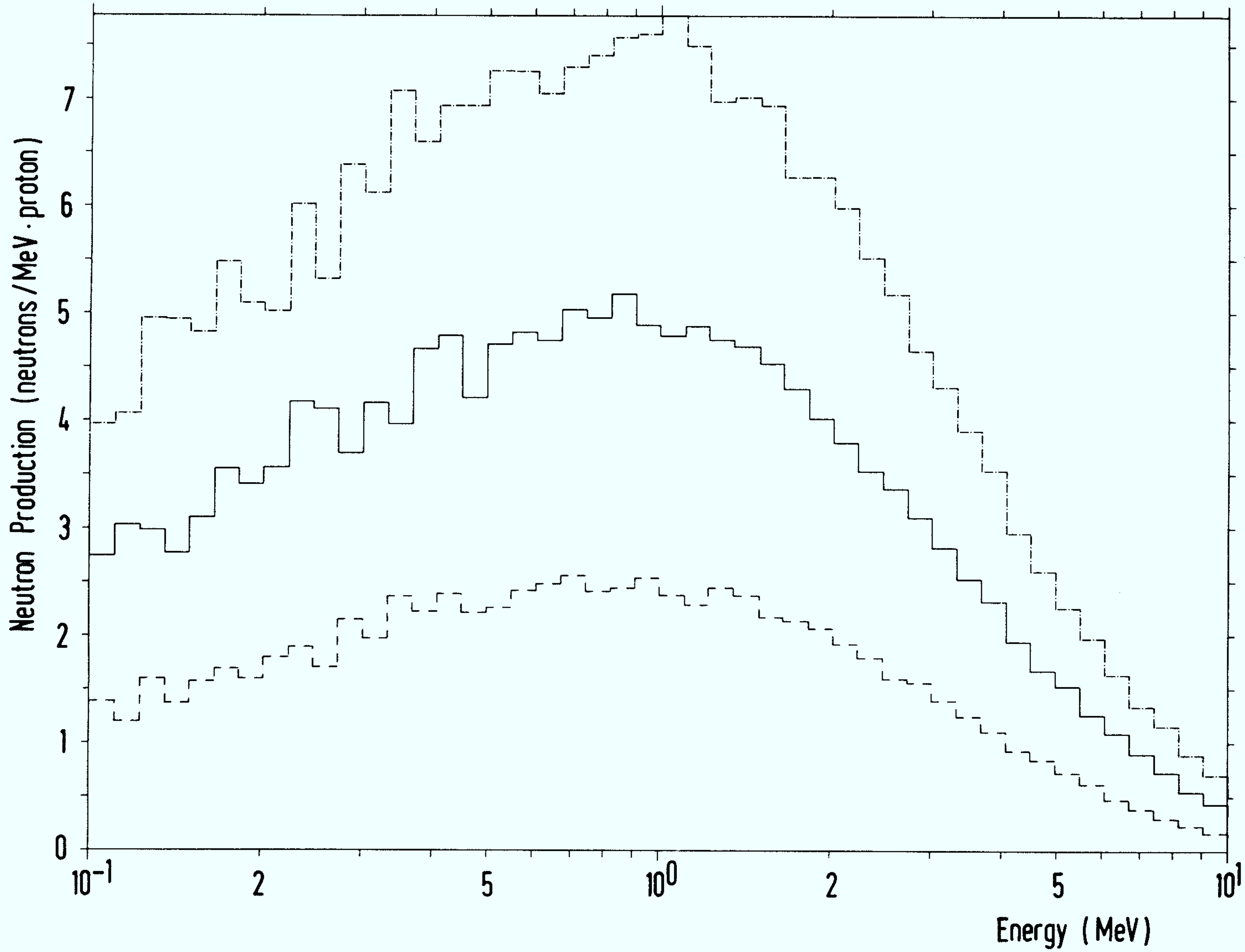

Figure 18: Evaporation neutrons with RAL-HEF model at proton beam energy E=540 MeV (dashed curve), E=960 MeV (solid curve) and E=1470 MeV (dashed-dotted curve) with B_0=14 MeV

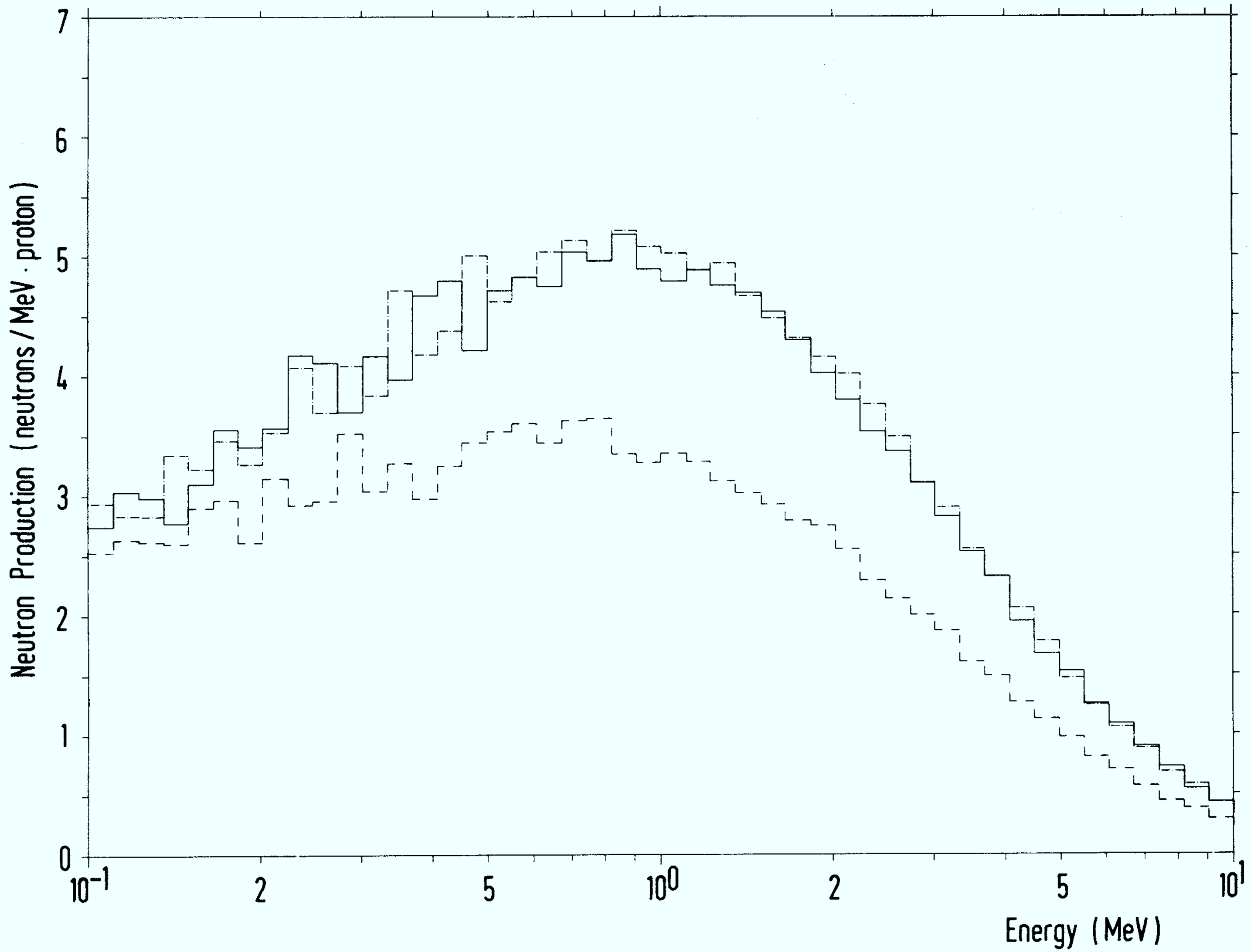

Figure 19: Evaporation neutrons with RAL-HEF model for target material of depleted uranium (solid curve), natural uranium (dashed curve), and lead (dotted curve) at 960 MeV proton-beam energy and B_0=14 MeV

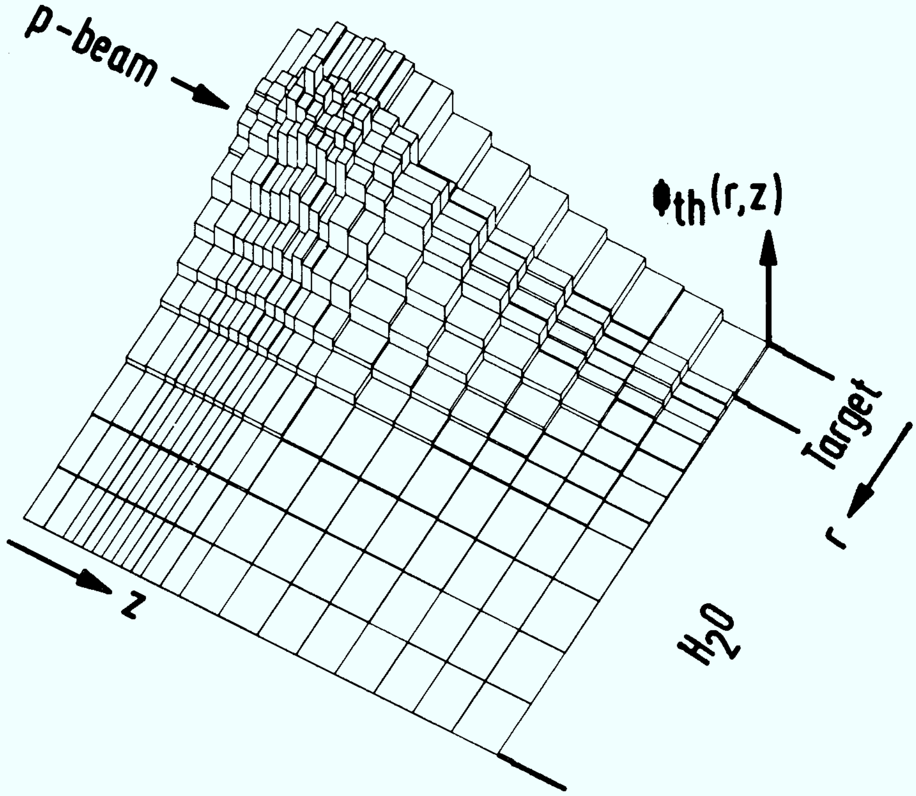

Figure 20: Thermal neutron flux distribution for the lead system in R-Z plane (incident proton beam energy 960 MeV)

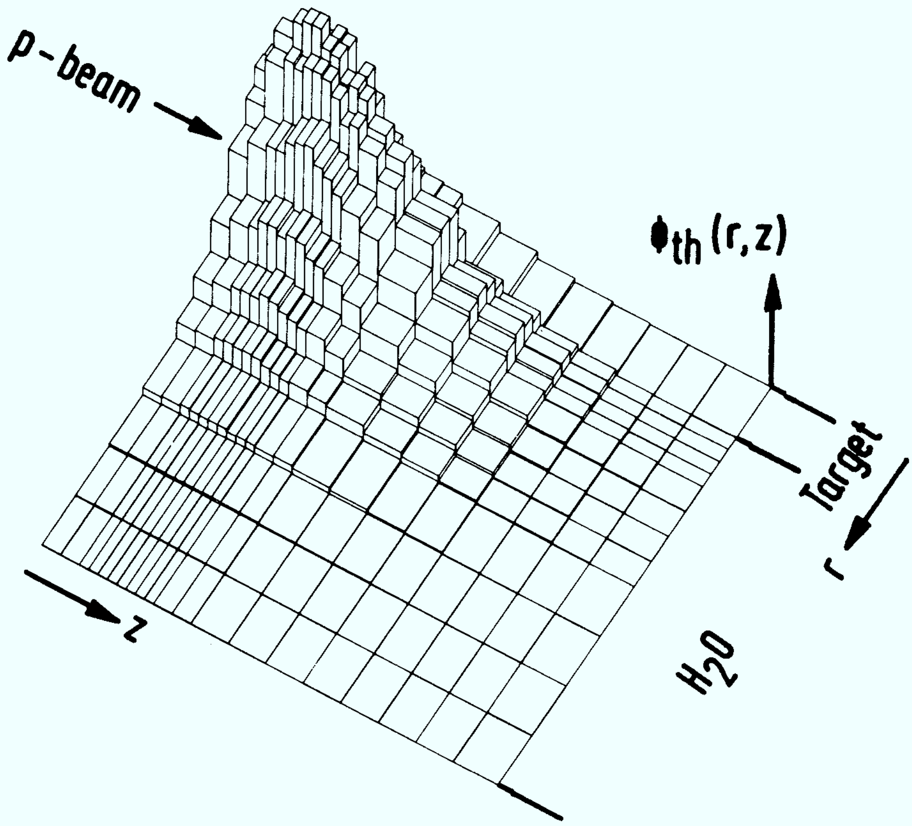

Figure 21: Thermal neutron flux distribution for the uranium system in R-Z plane (incident proton beam energy 960 MeV)

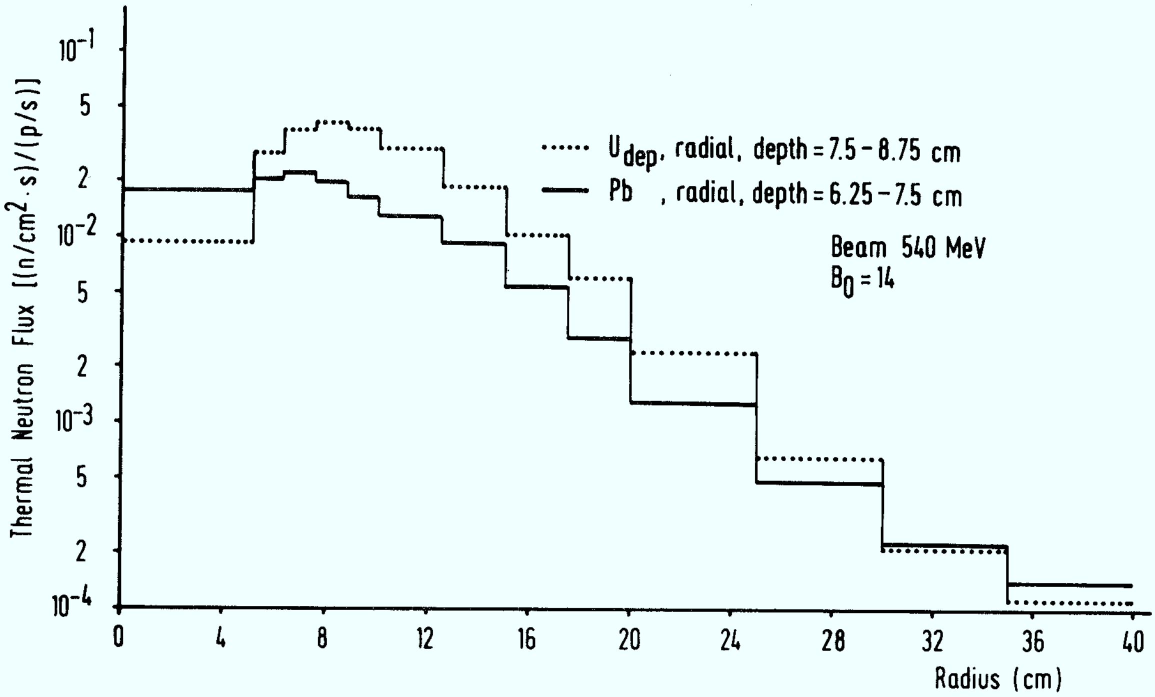

Figure 22: Radial dependence of thermal neutron flux in 7.5-8.75 cm depth interval for 540 MeV proton beam on depleted uranium and lead targets

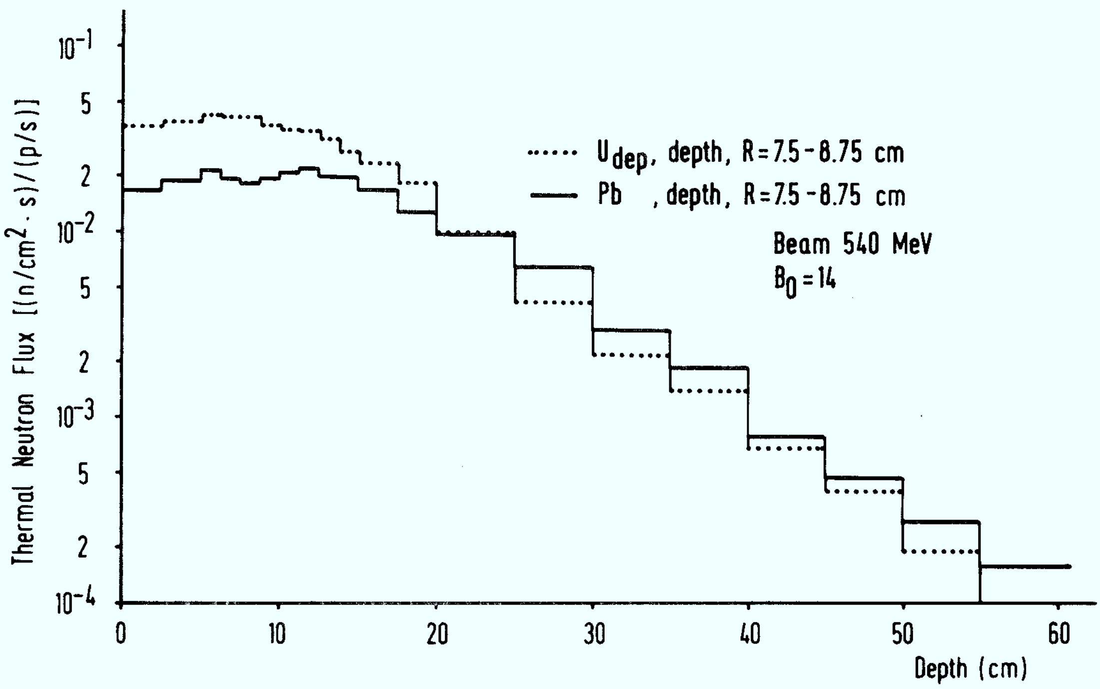

Figure 23: Depth dependence of thermal neutron flux in 7.5-8.75 cm radial interval for 540 MeV proton beam on depleted uranium and lead targets

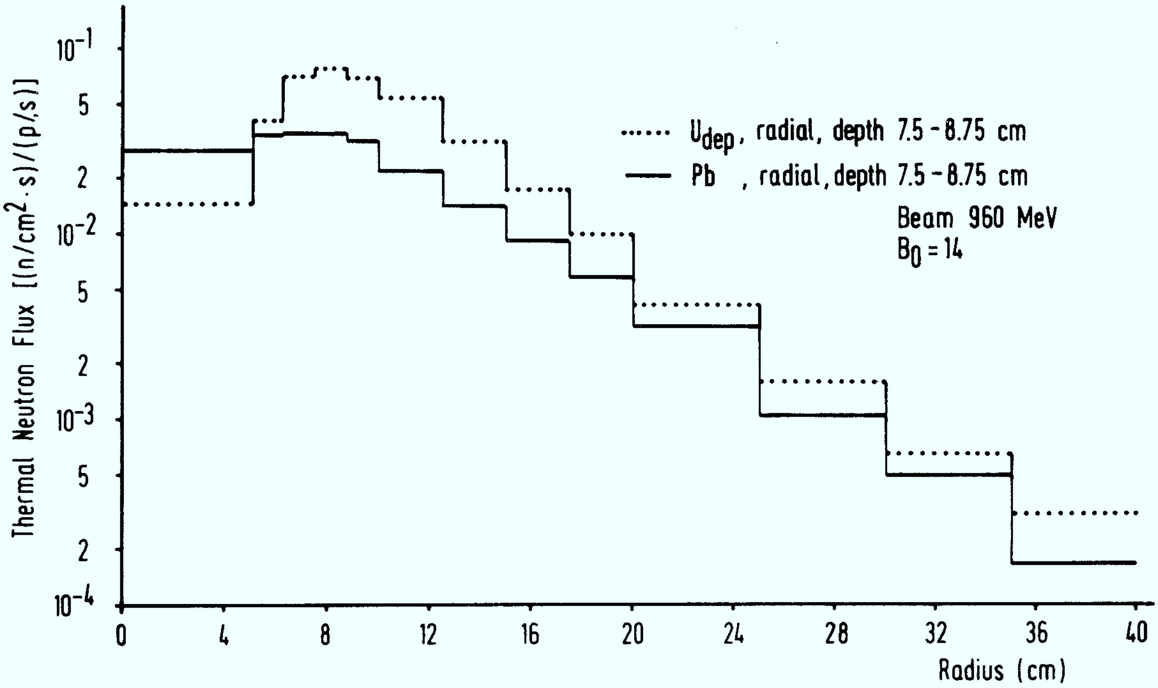

Figure 24: Radial dependence of thermal neutron flux in 7.5-8.75 cm depth interval for 960 MeV proton beam on depleted uranium and lead targets

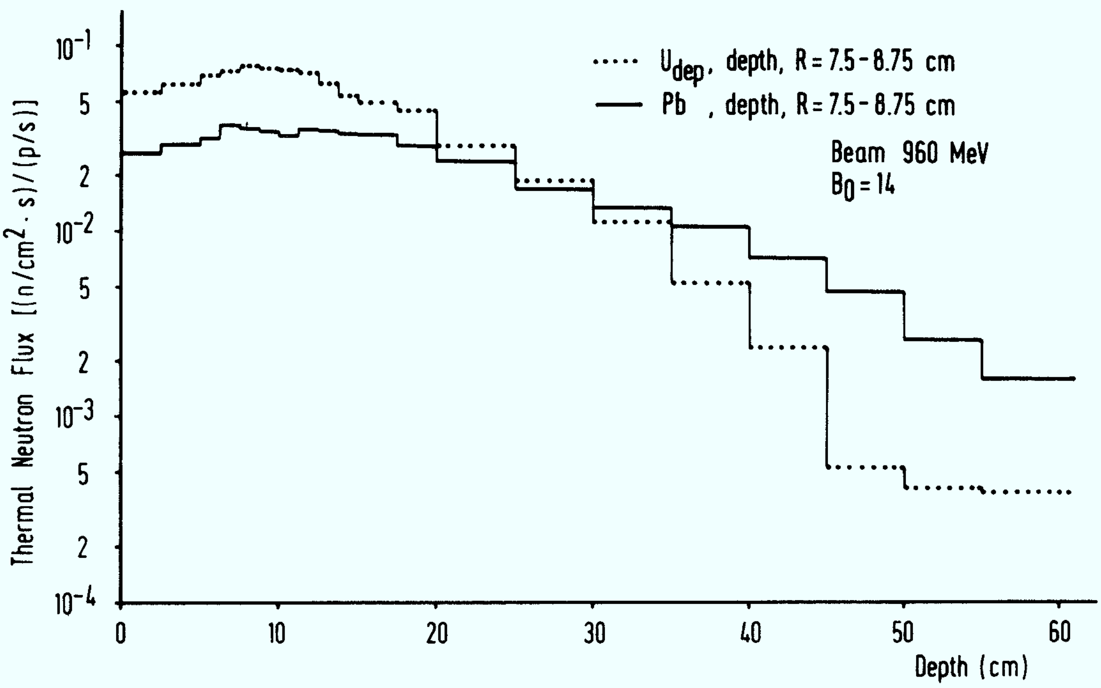

Figure 25: Depth dependence of thermal neutron flux in 7.5-8.75 cm radial interval for 960 MeV proton beam on depleted uranium and lead targets

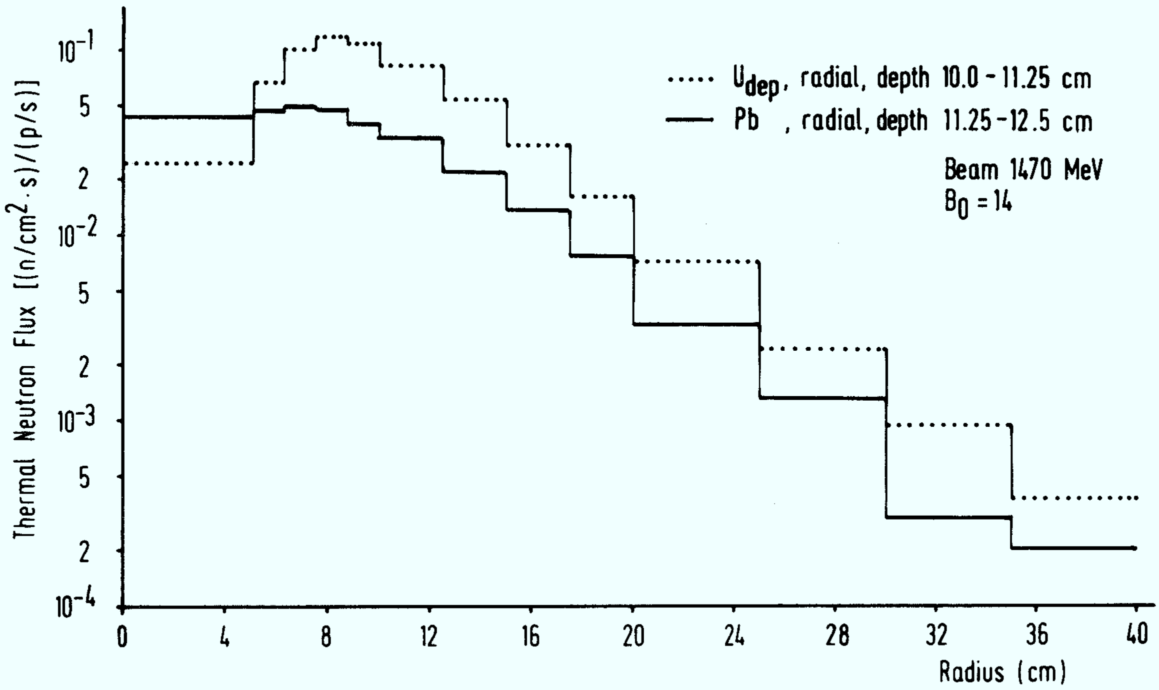

Figure 26: Radial dependence of thermal neutron flux in indicated depth intervals for 1470 MeV proton beam on depleted uranium and lead targets

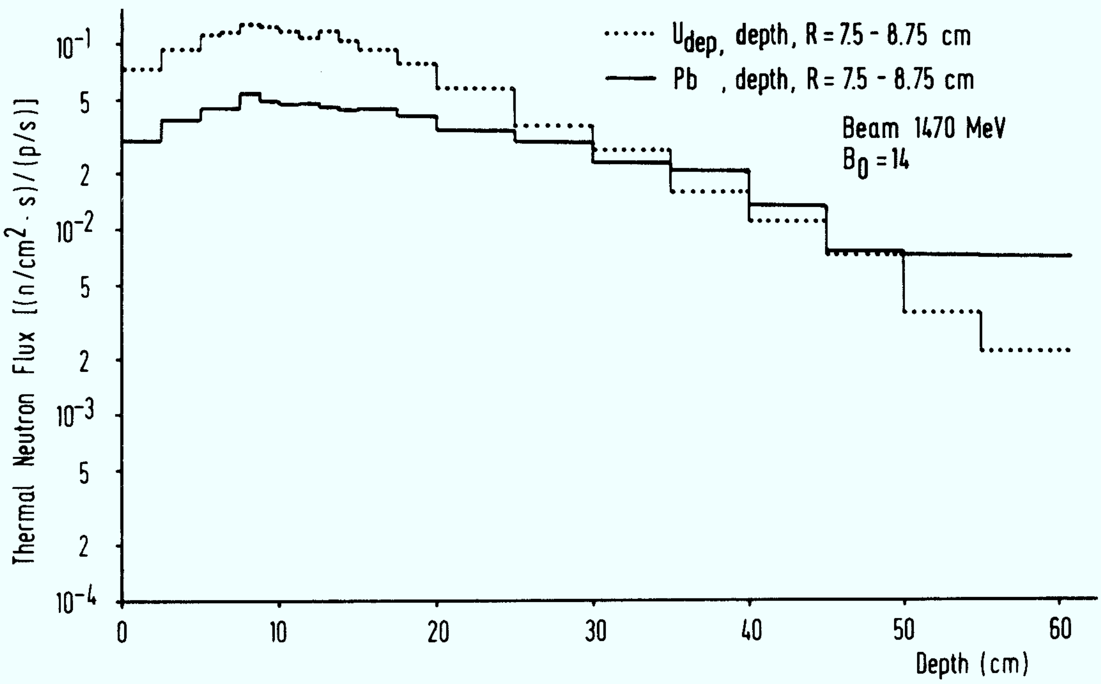

Figure 27: Depth dependence of thermal neutron flux in 7.5-8.75 cm radial interval for 1470 MeV proton beam incident on depleted uranium and lead targets

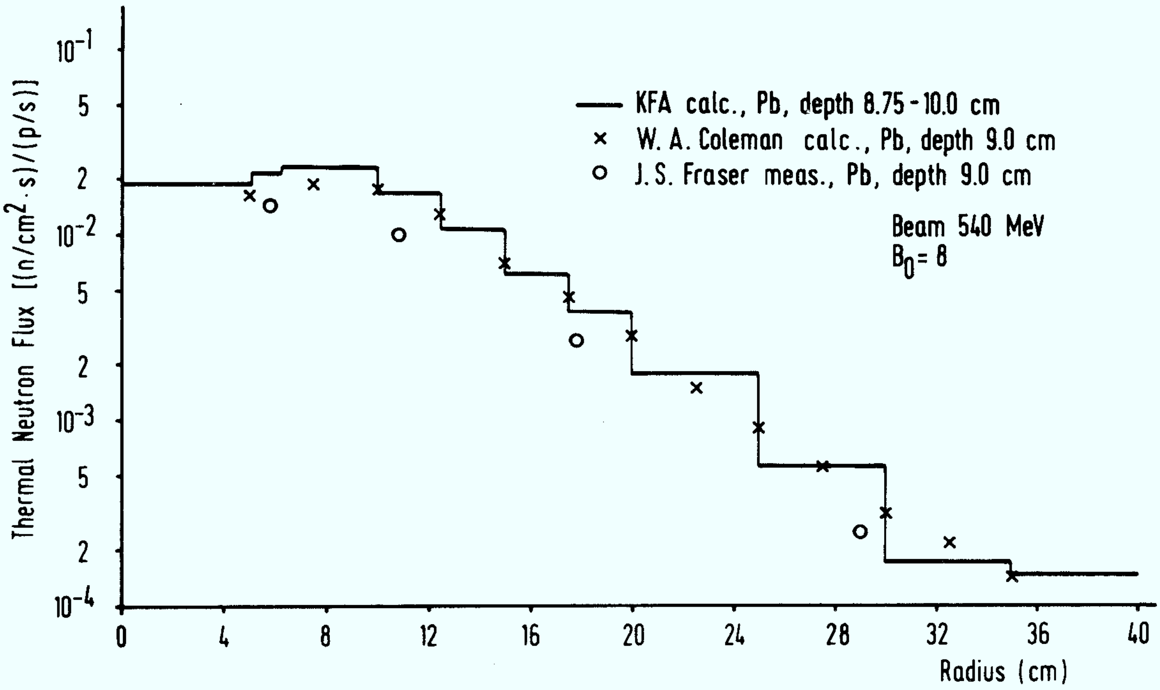

Figure 28: Comparison of calculations and measurement for radial distribution of thermal neutron flux, lead target, 540 MeV proton beam

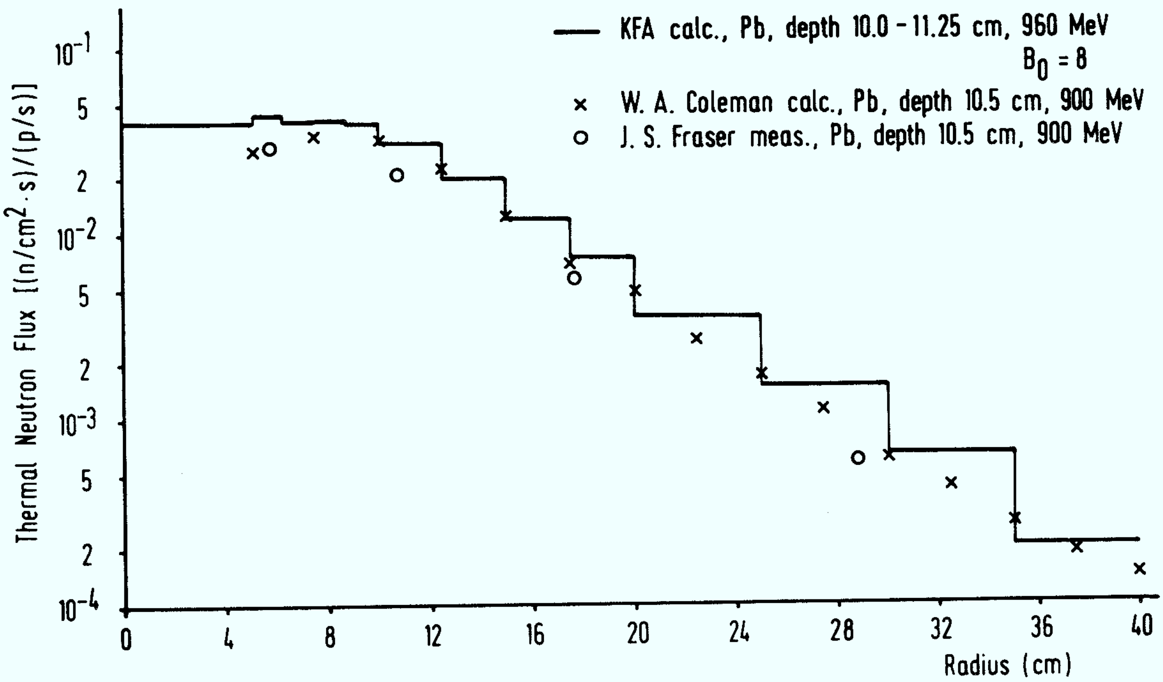

Figure 29: Comparison of calculations and measurement of radial distribution of thermal neutron flux, lead target, 900 MeV proton beam

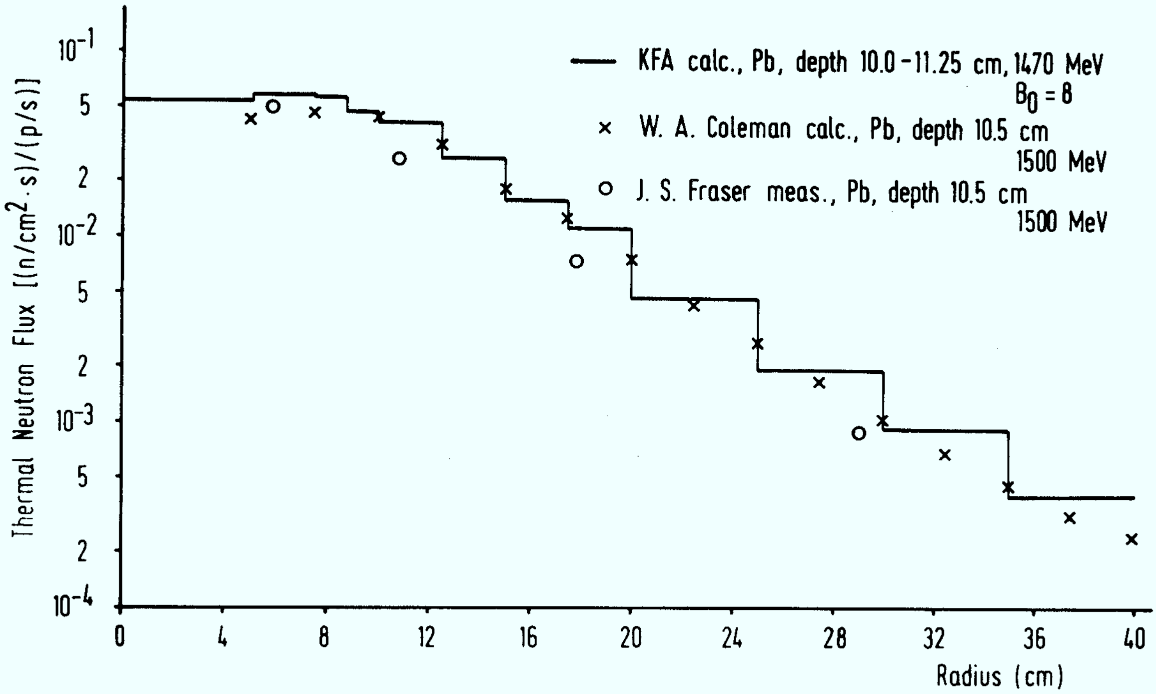

Figure 30: Comparison of calculations and measurement of radial distribution of thermal neutron flux, lead target, 1500 MeV proton beam

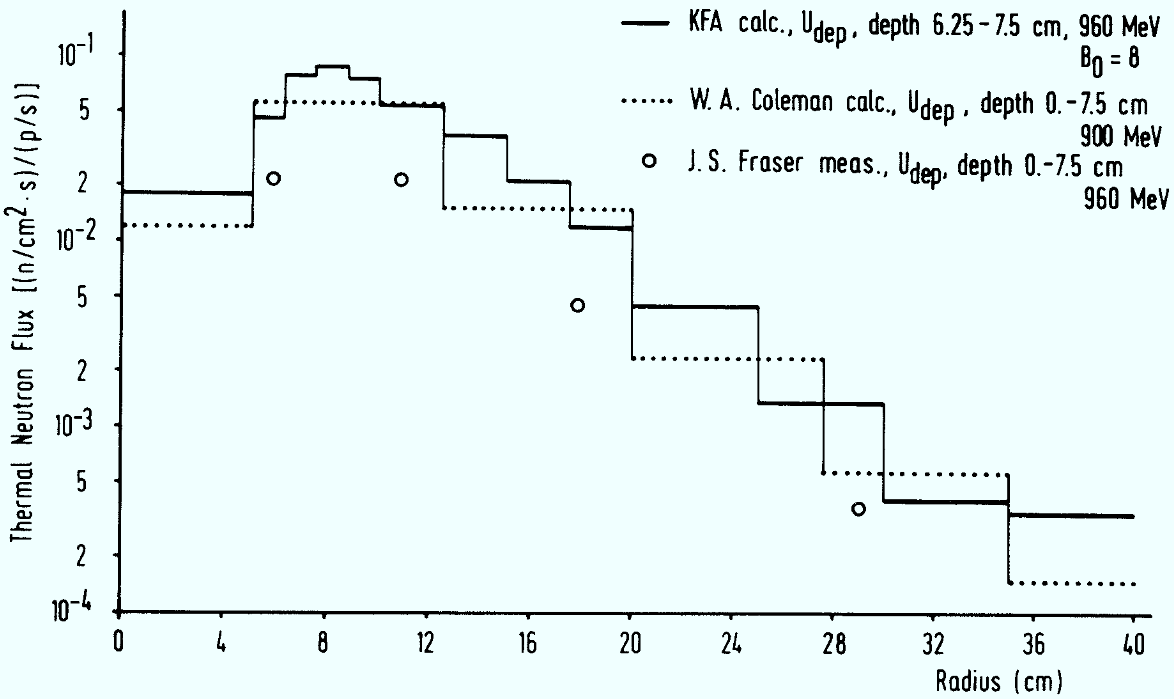

Figure 31: Comparison of calculations and measurement of radial distribution for thermal neutron flux, depleted uranium target, 960 MeV proton beam

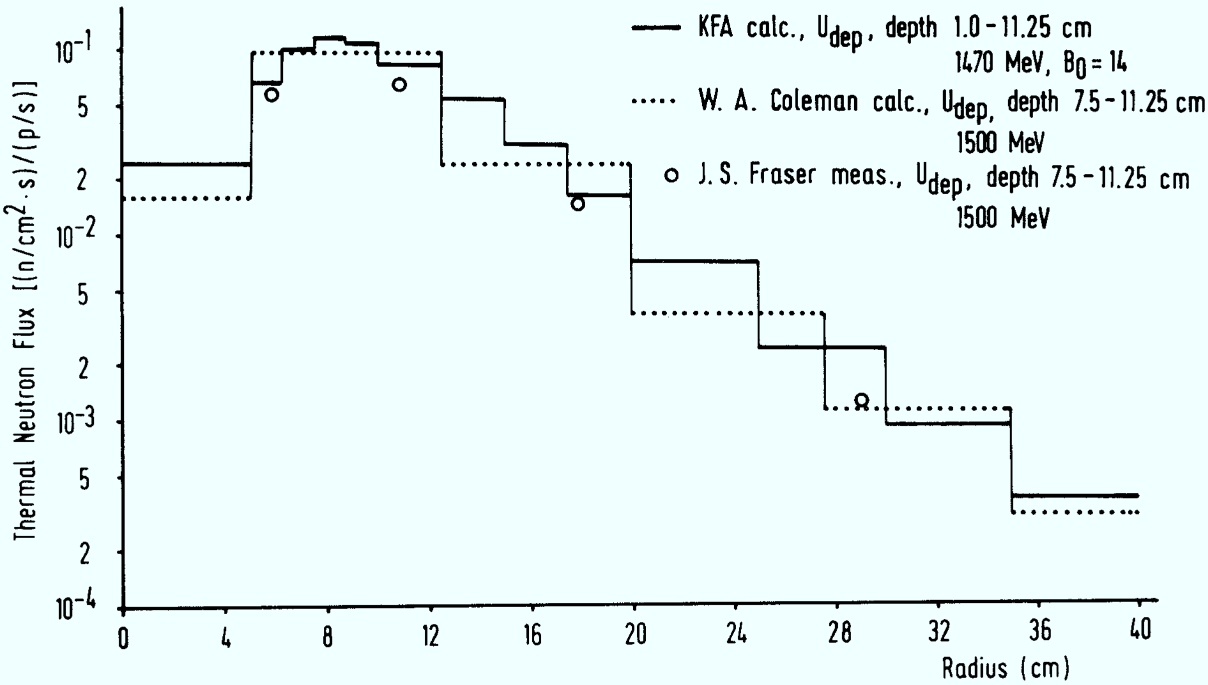

Figure 32: Comparison of calculations and measurement or radial distribution for thermal neutron flux, depleted uranium target, 1470 MeV proton beam

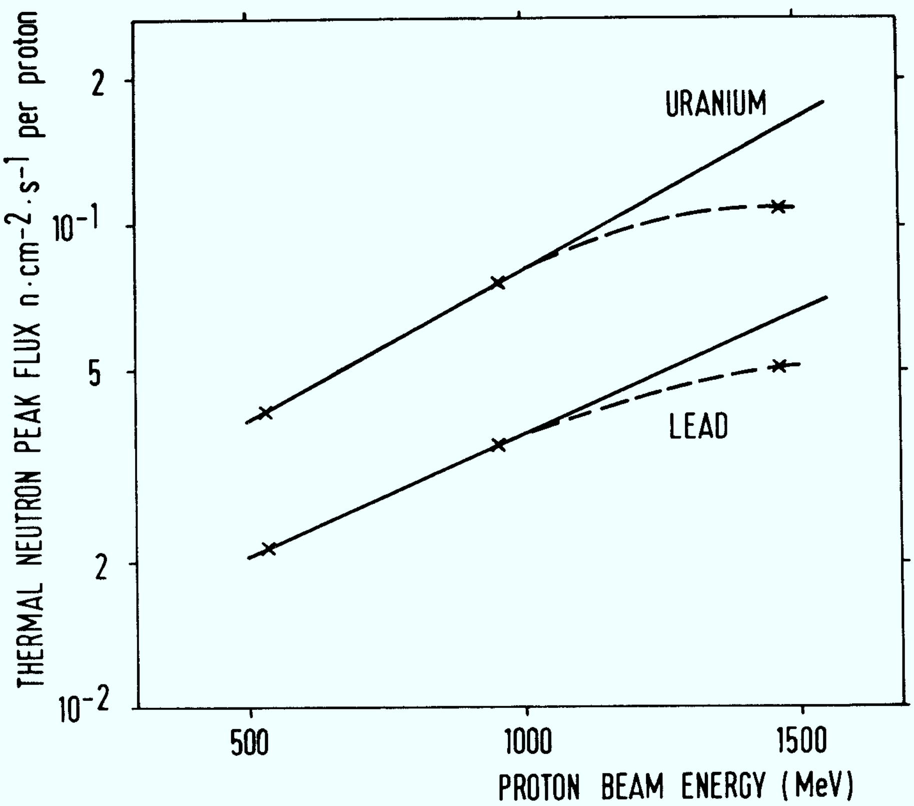

Figure 33: Thermal neutron peak fluxes per proton as a function of proton beam energy (540, 960, 1470 MeV) for lead and uranium targets with B_0=14 MeV

9 APPENDIX B

Tables

Table 1

Comparison of ORNL Fission Model with FERFICON Data[a]

Target	Proton E (MeV)	Quantity Compared	Theory/Exp.
1. Depleted U (3.2 ø x 30.5 cm)	480	Neutron captures in water bath	11.8/9.6[b] = 1.23[d]
Depleted U (37 rod array)	480	" "	14.1/17.7[b] = 0.82[d]
2. Depleted U (10 ø x 40.6 cm)	800	" "	27.2/25.3[c] = 1.08
Depleted U (37 rod array)	800	" "	28.6/28.8[c] = 0.99

(a) Calculated results from Alsmiller, et al. /11/

(b) Fraser, et al., FERFICON measurements at TRIUMF, reported at BNL Symposium /12/

(c) Russell, et al., FERFICON measurements at LASL, reported at ICANS-IV /13/

(d) Calculations of Fraser, et al. /12/, using NMTC without high-energy fission give theory/exp. ratios of 1.05 and 0.72 for cylindrical and array targets, respectively

Table 2

Fission Model Comparisons with Vassil'kov Experiments[a]

Fission Model	Proton E (MeV)	Quantity Compared	Theory/Experiment
JAERI[e]	660	U-238 captures	$\frac{44.9 \pm 5.1}{46 \pm 4} = 0.98$[b]
BNL[f]	660	" "	$\frac{38.3 \pm 5.2}{46 \pm 4} = 0.83$[d]
JAERI[e]	400	" "	$\frac{15.96 \pm 4.65}{22.1 \pm 2.4} = 0.72$[c]
BNL[f]	400	" "	$\frac{15.1 \pm 4.9}{22.1 \pm 2.4} = 0.70$

(a) Very large natural uranium assembly /14/

(b) Without high-energy fission in model, theory/exp. = 0.72

(c) Without high-energy fission in model, theory/exp. = 0.61

(d) Assuming depleted uranium with 33 % U-235 in calculations, theory/exp. = 0.88

(e) Ref. /6/

(f) Ref. /5/

Table 3

Calculated Nonelastic and Fission Cross Sections for Protons on U-238 Using RAL Fission Model

	Proton Energy		
	0.30 GeV	1.0 GeV	2.9 GeV
1. σ_{nonel} (barns)	1.75	1.92	1.88
2. σ_f (barns)	1.38	0.93	0.92
3. $P_f = \sigma_f/\sigma_{nonel}$	0.79	0.48	0.49

Table 4

Summary comparison of neutron production predicted by RAL and ORNL high-energy fission models, for proton beams on thin U-238 target

	Beam Energy (MeV)	Ratio: neutrons $\leq$12.5 MeV	Ratio: neutrons of all energies
1. ORNL* / RAL	300	1.23	1.19
	1000	1.28	1.22
	2900	1.26	1.19
2. ORNL (B_O = 8) / ORNL (B_O =15)	1000	1.22	1.17
3. ORNL (B_O = 8) / RAL (B_O = 8)	1000	1.14	1.12
4. RAL (with Fission)* / RAL (w/o Fission)	1000	1.08	1.07

*For standard B_O values incorporated in the models (B_O = 10 for ORNL, B_O = 14 for RAL)

Table 5

Calculations with and without High-Energy Fission (HEF) model

(Proton Beam Energy 960 MeV, Target Material Depleted Uranium)

	neutron production per proton		number or fissions in target per proton from		number of captures in uranium target per proton	number of neutron captures in H_2O per proton
	$\leq$15 MeV	>15 MeV	(a) neutrons $\leq$15 MeV	(b) neutrons and charged particles >15 MeV		
without HEF*	29.16	4.21	5.17	-	7.74	30.90
with HEF**	30.11	4.05	5.56	1.77	8.02	32.56
ratio of calculations with HEF vs. without HEF	-	-	1.08	-	1.04	1.06

* B_O parameter 8 MeV

**Rutherford Appleton Laboratory high-energy fission model (RAL model)

Table 6

Comparison of RAL- and ORNL-HEF Models for Different B_0 Parameters

(Proton Beam Energy 960 MeV, Target Material Depleted Uranium)

HEF Model	B_0 (MeV)	neutron production per proton $\leq$15 MeV	neutron production per proton >15 MeV	number of fissions in target per proton from (a) neutrons $\leq$15 MeV	number of fissions in target per proton from (b) neutrons and charged particles >15 MeV	number of captures in uranium target per proton	number of neutron captures in H_2O per proton
RAL	8	30.11	4.05	5.56	1.77	8.02	32.56
RAL	10	28.48	4.26	5.39	1.73	7.87	30.88
ORNL	10	31.73	4.49	6.18	1.93	8.72	35.23
RAL	14	26.03	4.43	5.03	1.71	7.01	29.03
ratio of							
RAL (B_0=14) vs. ORNL (B_0=10) (Standard)		0.82		0.81		0.80	0.82
RAL (B_0=10) vs. ORNL(B_0=10)		0.89		0.87		0.90	0.88

Table 7

Effect of Different B_0 Parameters (8,10 and 14 MeV) Using RAL-HEF Model (Proton Beam Energy 960 MeV, Target Material Depleted Uranium)

ratio of	neutron production per proton		number of fissions in target per proton from		number of captures in uranium target per proton	number of neutron captures in H_2O per proton
	$\leq$15 MeV	>15 MeV	(a) neutrons $\leq$15 MeV	(b) neutrons and charged particles >15 MeV		
B_o=8 MeV vs B_o=10 MeV	1.06	0.95	1.03	1.0	1.02	1.05
B_o= 8 MeV vs. B_o=14 MeV	1.16	0.91	1.11	1.0	1.14	1.12

Table 8

Comparison with Cosmotron Data (Fraser, et al. /27/)

Depleted Uranium Target, H_2O Captures per Incident Proton

incident proton energy (MeV)	experiment	HEF Model	B_O (MeV)	theory	theory vs. experiment
540	15.1±0.8	ORNL	10*	15.2±0.8	1.07
		RAL	14	13.5±1.1	0.81
960	32.3±1.6	ORNL	10*	33.7±1.0	1.04
		ORNL	10**	35.2±0.6	1.09
		RAL	10	30.9±0.3	0.96
		RAL	8	32.6±0.3	1.00
		RAL	14	29.0±0.3	0.89
1470	44.8±0.2	ORNL	10*	53.6±1.5	1.20
		RAL	14	46.0±0.4	1.03

* Calculations of Alsmiller et al. /11/

**KFA-IRE calculations using uranium cross sections with self-shielding corrections

Table 9

Neutron Production and Reaction Rates at Different Proton Beam Energies*

incident proton energy (MeV)	neutron production per proton		number of fissions in target per proton from		number of captures in uranium target per proton	number of neutron captures in H_2O per proton
	$\leq$15 MeV	>15 MeV	(a) neutrons $\leq$15 MeV	(b) neutrons and charged particles >15 MeV		
540	12.46	1.73	2.25	-	3.14	13.48
960	26.03	4.43	5.03	1.71	7.01	29.03
1470	42.03	7.65	8.03	-	11.99	46.03

*Calculated using RAL fission model with $B_o = 14$ MeV

Table 10

Comparison of Calculated Results for Lead, Depleted Uranium and Natural Uranium for the RAL-HEF Model (B_0=14 MeV at 960 MeV Proton Energy)

target material	neutron production per proton		number of fissions in target per proton from		number of captures in uranium target per proton	number of neutron captures in H_2O per proton
	≤15 MeV	>15 MeV	(a) neutrons ≤15 MeV	(b) neutrons and charged particles >15 MeV		
lead	19.46	4.30	-	-	0.502	18.75
depleted uranium	26.03	4.43	3.40 U238 1.63 U235	1.71	7.01	29.03
natural uranium	27.19	4.44	3.91 U238 4.07 U235	1.71	7.27	33.79
ratio of calculations						
natural U vs. depleted U	1.05		1.59	-	1.04	1.16
depleted U vs. lead	1.39	-	-	-	1.39	1.55

Table 11

Calculated thermal neutron peak fluxes for lead and uranium targets for two B_0 values at different incident proton beam energies

Energy MeV	Target	Evaporation Model	Thermal Peak Flux $n\ cm^{-2}s^{-1}$ per proton s^{-1}	Thermal Peak Flux $n\ cm^{-2}s^{-1}$ per 1 mA
540	Pb	B_0=8,no RAL	2.4×10^{-2}	1.5×10^{14}
	Pb	B_0=14, RAL	2.15×10^{-2}	1.34×10^{14}
	U_{dep}	B_0=14, RAL	4.15×10^{-2}	2.59×10^{14}
960	Pb	B_0=8,no RAL	4.7×10^{-2}	2.9×10^{14}
	Pb	B_0=14, RAL	3.55×10^{-2}	2.2×10^{14}
	U_{dep}	B_0= 8, RAL	8.9×10^{-2}	5.5×10^{14}
	U_{dep}	B_0=14, RAL	7.8×10^{-2}	4.8×10^{14}
1470	Pb	B_0=8,no RAL	6.25×10^{-2}	3.9×10^{14}
	Pb	B_0=14, RAL	5.1×10^{-2}	3.2×10^{14}
	U_{dep}	B_0=14, RAL	1.1×10^{-1}	6.9×10^{14}

Table 12

Comparison of Peak Thermal Neutron Fluxes in Moderator for U and Pb Targets

Beam Energy (MeV)	Lead HEF	Lead B_o	Depleted Uranium HEF	Depleted Uranium B_o	Thermal Peak Flux Ratio U/Pb
540	RAL	14	RAL	14	1.9
960	RAL	14	RAL	14	2.2
1470	RAL	14	RAL	14	2.2
540	NONE	8	RAL	14	1.7
960	NONE	8	RAL	14	1.7
1470	NONE	8	RAL	14	1.8
960	RAL	14	RAL	8	2.5
960	NONE	8	NONE	8	1.9

Table 13

Comparison of peak thermal flux ratios for different target materials and model assumptions, all for 960 MeV proton beam

Case 1			Case 2			Ratio of Peak Thermal Flux:
Target	HEF	B_o	Target	HEF	B_o	Case 1/Case 2
Pb	NONE	8	Pb	NONE	14	1.3
U_{dep}	RAL	8	U_{dep}	RAL	14	1.05
U_{dep}	RAL	8	U_{dep}	NONE	8	1.04
U_{nat}	RAL	14	U_{dep}	RAL	14	1.2

Table 14

Energy deposition produced in uranium target by 960 MeV proton beam (deposition from neutrons produced below 15 MeV not included)

	Energy deposition in MeV per proton	
	without High Energy Fission	with High Energy Fission
Primary Protons	261 ± 2 %	253 ± 2 %
Secondary Protons	184 ± 1.9 %	180 ± 1.6 %
Charged Pions	11.2 ± 5 %	12.2 ± 5.7 %
Neutral Pions	29.8 ± 5.6 %	27.8 ± 6.7 %
Muons	3.3 ± 6.8 %	3.45 ± 6.0 %
"Heavy" Particles*	16.2 ± 3.7 %	328.7 ± 1.4 %
Σ	517 ± 0.7 %	824 ± 0.6 %
Excitation Energy	11 ± 1.2 %	18.2 ± 1.3 %

*From recoil nuclei and heavy products (deuterons, tritons, ^{3}He and alpha particles) from evaporation